Contents

1 Introduction

Fibre-reinforced laminates are composite materials used in structural applications. Laminates are obtained by stacking a number of thin layers (called *ply*, or *lamina*) of fibres and matrix and consolidating them into the desired thickness. Fibre orientation in each layer as well as the stacking sequence of various layers can be controlled to generate a wide range of physical and mechanical properties for the composite laminate [1].

While the high ratio of mechanical strength to specific weight of some fibre-reinforced composites makes them suitable for aerospace applications, for example, their high ratio of mechanical strength to thermal conductivity makes them very interesting for cryogenic applications in accelerators. In the case of the Large Hadron Collider (LHC) [2], the support posts of the superconducting magnets are made of carbon and glass fibre composites supporting a high compressive strength with a minimum of heat leakage [3].

Another application in the LHC, which is the subject of this report, is the tuning structure of the superconducting 400 MHz cavities. They are tuned to the required resonant frequency by changing their axial length [4]. This is accomplished by an actuator mounted outside the cryostat at room temperature. The actuator is connected to the cold (4.2 K) niobium-coated copper cavity by a rigid tuning structure which has to withstand relatively high tensile tuning forces and which provides the necessary thermal insulation. These conflicting requirements are, for our geometry, best met by a carbon-fibre-reinforced epoxy tube (an epoxy is a thermoset polymer).

The particularity of our application is the large temperature difference on the carbon-fibre tube which leads to high local temperature gradients. This varying temperature in combination with time-dependent tensile load due to the tuning mechanism and exposure to ionizing radiation caused by beam losses is likely to reduce the life expectancy of the tuning structure.

Data on fatigue tests of carbon-fibre-reinforced composites have been reported in the literature [5]–[8]. There, the samples have been at cryogenic temperatures without a temperature gradient across the samples, which differs from our application. Also, the number of cycles is of the order of 5×10^6 which is not enough for reliable operation for the lifetime of the LHC.

In the work presented here we investigate a carbon-fibre tube for the cavity tuning structure, and in particular, we study its fatigue behaviour in the presence of a large temperature gradient for a very high number of load cycles. This combination represents the originality of our investigation.

Section 2 starts with a description of the cavity and its tuning requirements which leads to the specification of the the carbon-fibre tube. After considering other materials, we discuss the choice of carbon fibre, and finally the construction of the tube is presented. In Section 3, a model of the tube is analyzed with respect to stresses and strains, and the temperature distribution over the tube is estimated. We also attempt a failure analysis. Section 4 describes the test apparatus, the test methods and the promising results of the long duration fatigue tests. Concluding remarks are made in Section 5.

2 Tuning and the Carbon-Fibre Tube

2.1 Cavity Tuning

The superconducting 400 MHz cavity of the LHC is fabricated from 2.5 mm thick high-purity copper sheet metal, coated inside with a thin (1 μm) film of niobium. After cold forming the cavity half-shells (∅ 690 mm) and the large diameter beam tubes (∅ 300 mm) are joined by electron-beam welding.

Fabrication of several cavities has shown that the resonant frequency just after welding is correct within 0.5% at least. Tuning to the correct frequency is done by plastic deformation in the axial direction. Depending on the manufacturing tolerances, this can be a compression or an elongation of the cavity. This first tuning is done at room temperature with atmospheric pressure inside the cavity. Therefore, the change of resonant frequency due to cool down and vacuum pressure has to be taken into account.

Further tuning is done in the elastic range of the axial length variation (2 mm). The tuning displacements originate in the tuning mechanism (Fig. 2.1). The tuning forces are transmitted

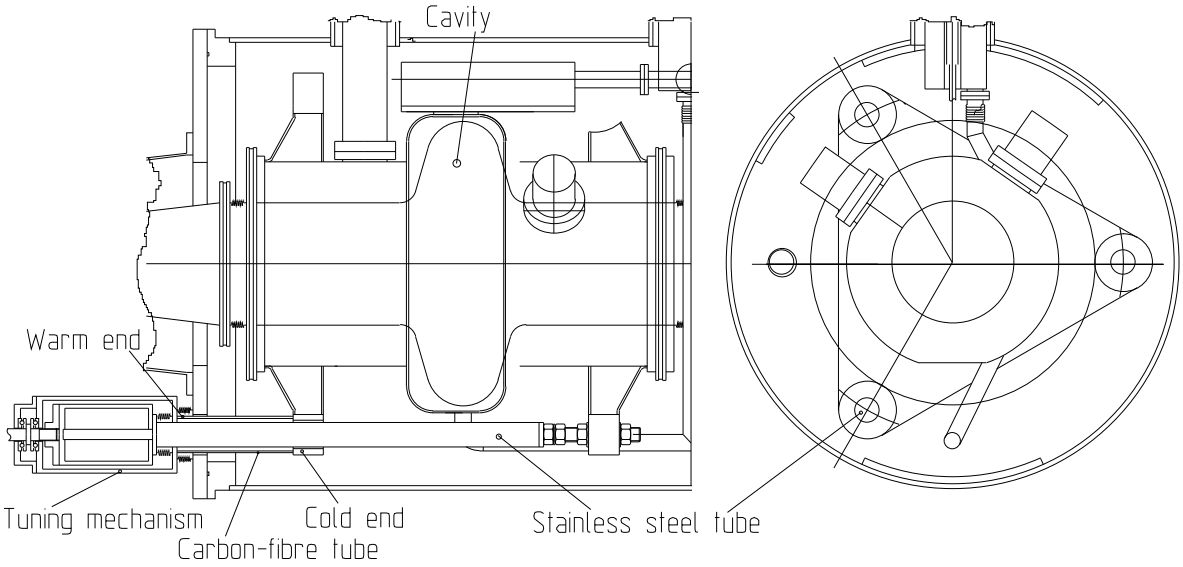

Figure 2.1: LHC RF cavity tuning system

to the cavity with a rigid structure consisting of sturdy flanges, stainless-steel tubes, and carbon-fibre tubes. Three tubes are foreseen to return the forces (the tuning system is at present (1997) under revision).

Pumping a vacuum in the cavity results in an axial compression of about 0.5 mm [9]. In order to make use of the total elastic range of 2 mm the cavity has to be elongated by the tuner. This determines the directions of stress. The cavity and the connected flanges are under tensile stress, and the parts returning the forces under compressive stress. Clearly, the cavity body is always under tensile stress.

The axial spring constant of the cavity is about 20 kN/mm. Thus, the maximum force to cover the elastic range is 40 kN. Taking a safety factor of 2, we specify 80 kN, resulting in about 27 kN for each tube.

The tuning sensitivity is 240 kHz/mm. The total dynamic tuning range is 480 kHz which is 0.12% of the fundamental resonant frequency.

During operation of the LHC, fine tuning is required to compensate for the varying beam current and various microphonic perturbations. The corresponding length variation of the cavity is estimated to be 0.1 mm. These variations have to be relatively fast, of the order of up to 100 Hz (microphonics of about 90 Hz have been observed in the LEP superconducting cavities). This permanent tuning motion puts an oscillatory load on all components of the tuning system and may lead to failures caused by fatigue.

The subject of this report is the 290 mm carbon-fibre tube which spans from cryogenic to room temperatures. The choice of its cross-section is a compromise between the requirements of high mechanical stiffness and good thermal insulation.

In addition to the external mechanical loads, it is stressed internally by temperature gradients. The tube has to be resistant to ionizing radiation which is estimated to be 180 Gy after 20 years [10].

The specification of the tube is summarized in Table 2.1.

Table 2.1: Specification of the tube

Static tensile load	27 kN
Dynamic load at 100 Hz	1 kN
Number of dynamic load cycles	5×10^9
Axial spring constant	$\geq$ 70 kN/mm
Maximum dose of ionizing radiation	180 Gy
Heat flow rate [11]	$\leq$ 1.5 W

2.2 Comparison of Materials

It is interesting to compare the chosen material (high-strength carbon fibre) to other material which could be considered for this application (see Table 2.2); the fatigue strength of steel is

Table 2.2: Comparison of unidirectional laminates and steel [5, 12] (room temperature values)

Properties $\Rightarrow$ $\Downarrow$ Material $\Downarrow$	Fatigue strength σ_{fat} [MPa]	Therm. cond. λ [W/(m·K)]	Young's modulus E_{11} [GPa]	$\sigma_{\text{fat}}/\sigma_{\text{ult}}$ [%]
Steel (50CrV4)	720	21	210	60
Carbon (HM)	800–1000	30	240–330	50–70
Carbon (HS)	1300–1400	5	120–180	70–80
S-glass	250–280	0.7	55–65	15–30
Aramid (Kevlar 49)	800–1000	20	75–85	60–70

given for a survival probability of ninety per cent [12]. For the fibre-reinforced laminates a great variety of different strength values can be found in the literature, because of different fibre matrix combinations and the strong dependence of the material properties on the production process. All data on fibre-reinforced composites are taken from Ref. [5] which gives an excellent overview of fatigue tests at cryogenic and room temperatures.

Carbon-fibre-reinforced laminates and Kevlar have extremely high **fatigue strength** whereas S-glass has the lowest. In particular, high-strength carbon-fibre (HS) material has an outstanding ratio of fatigue strength over ultimate strength. This is very important since the number of load cycles in our application is extremely high and it seems risky to use S-glass because this material loses at least 70% of its strength after only 10^6 load cycles. No data on longer fatigue tests has been found.

Thermal conductivity varies by more than one order of magnitude. S-glass has the lowest thermal conductivity at room temperature. But at temperatures below about 40 K, high-strength carbon fibres have even lower thermal conductivity than S-glass. The difference in thermal conductivity between high-modulus and high-strength carbon-fibre-reinforced materials is due to the heat treatment of the fibres. For ultra-high modulus fibres the thermal conductivity can increase by two orders of magnitude during the treatment at about 3000°C. Therefore high- and ultra-high modulus carbon-fibre composites are less interesting for us, although they have the highest stiffness. Another disadvantage of high-modulus carbon-fibre (HM) material which is not listed in Table 2.2 is the extremely low strain-to-failure of the fibre (less than 0.5 per cent). This can cause rupture of fibres if high stress concentrations occur in the tube's wedged end section, for example.

The **Young's moduli** of Kevlar and S-glass are low compared to those of steel and carbon fibres. Therefore larger cross-sections would be necessary to fulfil the stiffness requirements.

When looking for a material with good fatigue properties in combination with a relatively low thermal conductivity and a relatively high stiffness, high-strength carbon-fibre-reinforced material is the best choice. One needs to check, however, whether this material possesses sufficiently high radiation resistance. In particular the matrix has to be chosen with care. Some of the polymeric matrix materials become brittle as a result of chain-cracking when exposed to radiation. This can weaken their properties considerably.

A carbon-fibre-reinforced epoxy was tested at CERN in 1995 [13]. It withstood a dose of 60 MGy which is more than five orders of magnitude more than the estimated dose for the LHC. However, this test did not consider prestressed material, and it was found in the literature that prestressed laminates are much less radiation resistant. Burnay [14] investigated the effect of prestressing on the behaviour of carbon-fibre-reinforced plastics under gamma irradiation. He found considerable losses in inter-laminar shear strength at a dose as low as 2 MGy. Although Burnay did not examine the same epoxy, his unstressed samples were three to four times more radiation resistant than his prestressed samples. Therefore the value found at CERN should be used with care whenever the material is subjected to stresses. The critical dose found by Burnay is higher by more than four orders of magnitude than the dose in the LHC (Table 2.1). Radiation damage is therefore considered to be no problem in our case.

2.3 Tube Construction

High-strength carbon-fibre-reinforced laminates have anisotropic properties. The stiffness of a single ply in the fibre direction and in the transverse direction varies by more than one order of magnitude. The same is true for the coefficient of thermal expansion. As a result of high temperature differences between the stress-free state of the laminate at curing temperature (about 110°C) and the temperature at the cold end of the tube (about 15 K), considerable thermal strains and stresses occur.

Because high stiffness is required in the direction of the tuning forces, most of the fibres should be aligned with a small angle to the load axis. The end sections of the structure need

to be designed in such a way as to avoid stress concentrations; no holes should be drilled and no abrupt changes in cross-section should occur, since these geometries promote failure propagation under fatigue loading. Often, wedged end sections are used to provide a smooth force transition.

Since some bending load might occur, a cross-section with relatively high bending resistance should be chosen; a hollow cylinder is preferred to a rod. A cylinder can be manufactured

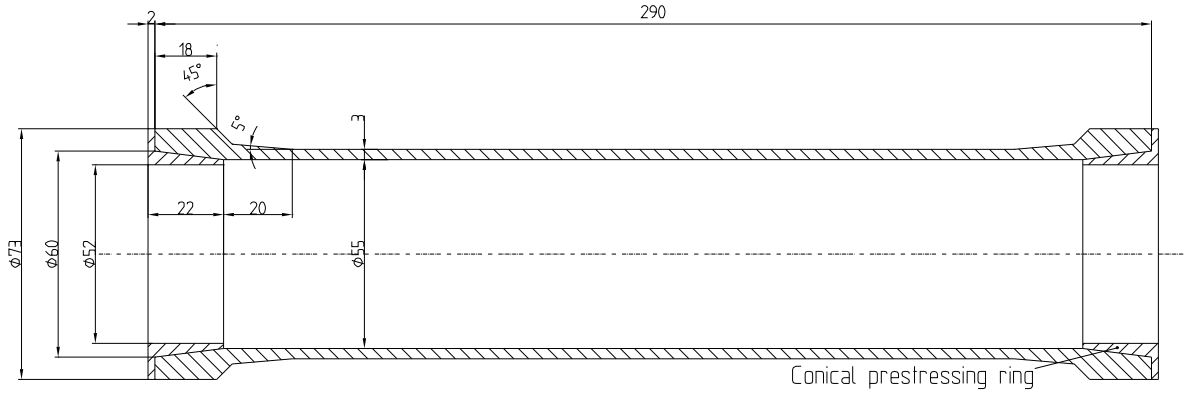

Figure 2.2: Geometry of the prototype tube

by the *filament-winding* technique [1] with fibre angles between near 0° and 90° relative to the axis of the cylinder. Several layers with different materials can be combined.

In co-operation with *Stesalit AG*, Zullwil, Switzerland, a carbon-fibre-reinforced tube was designed and manufactured (see Fig. 2.2). The tube consists of four cross-layers, with winding angles of $\pm 18^\circ$ relative to the axis. The fibre is a high-strength carbon fibre (HS), with an elastic modulus of 235 GPa (elastic modulus of the fibre itself) and a strain-to-failure of 2.1% (*Torayca* T700 SC12K). The epoxy matrix (*Ciba-Geigy* LY 556, HY 917, DY 070) was chosen because of its radiation resistance as tested at CERN [13]. The elastic modulus of a single ply in fibre direction is 143.5 GPa. Each ply contains a volume of 65% of fibres and 35% of matrix.

A long curing time (for the polymerization reaction of the epoxy) of 12 hours at a temperature of 100–110°C was chosen to reduce the thermal stresses due to cool down. The elastic properties of the ply, the thermal expansion coefficients, and the ply-strength values, all provided by the manufacturer and all valid at room temperature, are listed in Table 2.3. At CERN we have measured the contraction of the tube when immersed into liquid nitrogen at 77 K. The tube (length 290 mm) shortens by 0.02 mm which results in a mean axial thermal expansion coefficient for the temperature range from 290 K to 77 K of $\bar{\alpha} = 3.2 \times 10^{-7}$. A steel tube with the same geometry would shorten by 0.7 mm when cooled down from 290 K to 77 K. This is 35 times more than for the carbon-fibre tube.

At both extremities of the tube three layers of quasi-isotropic glass fleece are merged between the four cross-layers of carbon-fibre-reinforced epoxy to obtain wedged end sections (see Fig. 2.3). Stress concentrations are minimized by the low-modulus glass fleece between the relatively stiff carbon-fibre-reinforced plies. This is very important for components under fatigue loading, since damage occurs first at areas of high stress and then propagates (for example a hole in a plate).

The tube is connected to the stainless steel flanges with **wedge fittings**. See Figure 2.3. The cone-shaped extremities of the tube are clamped between a conical prestressing ring and

an outer ring. This results in radial compression of the tube which reduces considerably the axial shearing forces at the critical interface of the glass fleece and the carbon-fibre cone.

Table 2.3: Ply properties measured at room temperature [15]. The thermal expansion coefficients of the ply were calculated from the measured values of the fibre and the matrix.

Young's modulus in fibre direction	E_{11}	143.5 GPa
Young's modulus in transverse direction	E_{22}	9.5 GPa
Ply-shearing modulus	G_{12}	6.15 GPa
Major Poisson ratio	ν_{12}	0.32
Minor Poisson ratio	ν_{21}	0.0021
Thermal expansion coefficient in fibre direction	α_1	-8.0×10^{-7} 1/K
Thermal expansion coefficient in transverse direction	α_2	3.7×10^{-5} 1/K
Mean axial thermal expansion coefficient of the tube (winding angle $18°$) for cooldown from 290 K to 77 K	$\bar{\alpha_x}$	3.2×10^{-7} 1/K
Tensile strength in fibre direction	S_L	2550 MPa
Tensile strength in transverse direction	S_T	68 MPa
Compressive strength in fibre direction	$S_{L,c}$	-1100 MPa
Compressive strength in transverse direction	$S_{T,c}$	-170 MPa
In-plane shear strength	S_{SS}	80 MPa

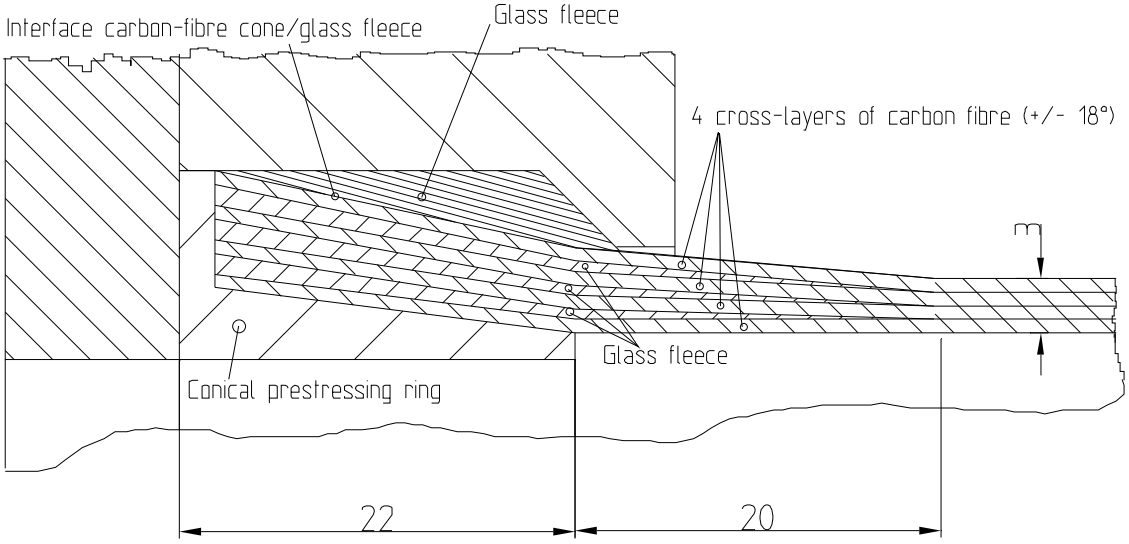

Figure 2.3: Wedged end section of the tube (Stesalit AG, Switzerland, 1995)

3 Model

In the literature a variety of articles on stress analysis of orthotropic tubes under different mechanical and thermal loading conditions can be found [16]– [22]. However, only radial temperature gradients, for example due to a hot liquid passing through a tube, are treated in the cited articles. In our particular problem temperature varies with the axial coordinate.

We want to estimate stresses and strains in our tube that are caused by the mechanical and the axially varying thermal loads with a simple model of the tube (see Fig. 3.1). We neglect the wedged end sections and consider here only an effective tube length of $L = 250$ mm. Mechanical strains are caused by the applied tensile tuning forces (F) and by the thermal load.

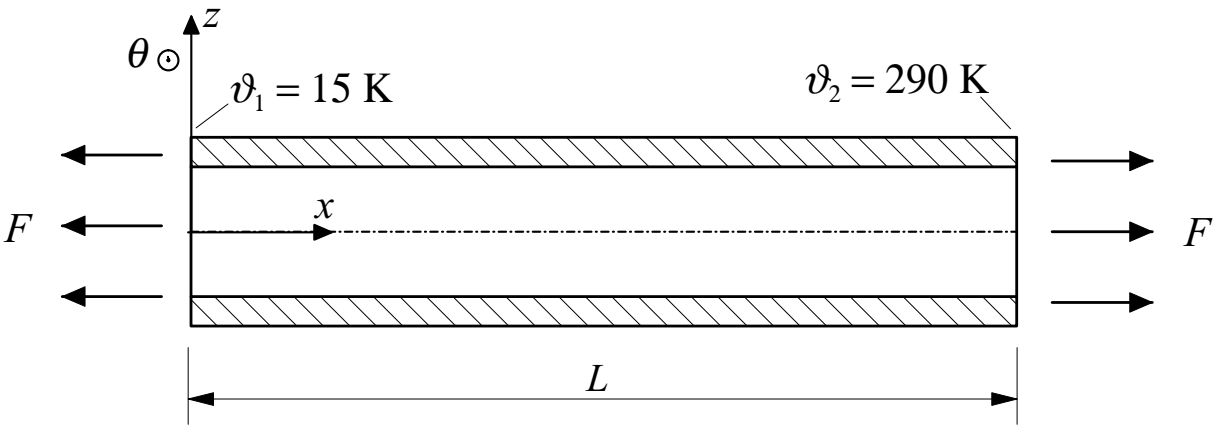

Figure 3.1: Cylindrical tube with tensile tuning force (F) and axially varying temperature (ϑ_1, ϑ_2). The difference between the polymerization temperature (100–110°C) and the working temperature (ϑ_1, ϑ_2) leads to additional mechanical stresses in the laminate.

The thermal load appears due to restrictions imposed by various layers against their free thermal expansion [1]. Since the curing temperature is considerably higher than the working temperature of the laminate, these restrictions can cause relatively high mechanical stresses in the tube.

3.1 Stress Analysis

The **temperature distribution** over the tube length is calculated in order to determine the strains, caused by the thermal load. According to Smith et al. [23], "...stress analysis procedures for composite materials can be rather complex ... Because composite materials are fabricated by the lamination of highly anisotropic plies, a nearly infinite variety of directional moduli and strengths can be achieved."

We consider an orthotropic tube, with cylindrical cross-section A_s and length L, under thermal load. The differential equation of conduction of heat in an orthotropic solid can be written after Carslaw [24]

$$\frac{1}{z}\frac{\partial}{\partial z}\left(\lambda_1 z\frac{\partial \vartheta}{\partial z}\right) + \frac{1}{z^2}\frac{\partial}{\partial \theta}\left(\lambda_2\frac{\partial \vartheta}{\partial \theta}\right) + \frac{\partial}{\partial x}\left(\lambda_3\frac{\partial \vartheta}{\partial x}\right) - \rho c\frac{\partial \vartheta}{\partial t} = 0\ , \tag{3.1}$$

where $\lambda_1, \lambda_2, \lambda_3$ are the temperature-dependent thermal conductivities in radial (z), angular (θ) and axial (x) directions, respectively. The temperature ϑ can be a function of all three coordinates, t is the time, ρ is the average density, and c the specific heat of the material.

Heat flow takes place in the x-direction only. There is no heat flow in the radial direction, since the tube is surrounded by a vacuum and therefore convection is negligible. Owing to the low temperatures of the tube, radiation (*Stefan–Boltzmann law*) is negligible. There is no over-all heat flow in the circumferential direction because the laminate is balanced (the same amount of fibres is aligned with $+\alpha$ and $-\alpha$ angles towards the x-axis).

The temperatures at both ends of the tube are assumed to be constant.

With these assumptions Eq. (3.1) becomes

$$\frac{\mathrm{d}}{\mathrm{d}x}\left(\lambda_3(\vartheta)\frac{\mathrm{d}\vartheta}{\mathrm{d}x}\right) = 0 \ , \tag{3.2}$$

where the temperature dependence of the thermal conductivity is given as a fourth order polynomial, resulting from a fit to experimental data (see Appendix A).

The boundary conditions are

$$\vartheta(0) = \vartheta_1 \ , \quad \vartheta(L) = \vartheta_2 \ . \tag{3.3}$$

The cold end of the tube is joint to a steel flange which we estimate to be at about 15 K (see Fig. 2.1). Solving Eq. (3.2) with $\vartheta_1 = 15$ K, $\vartheta_2 = 290$ K, and $L = 250$ mm yields the temperature distribution as a function of x (Fig. 3.2). See Appendix A for the detailed calculations.

The dotted line in Fig. 3.2 represents the solution of the differential equation of conduction of heat, whereas the continuous line is a fit to the solution, using a least-square method. This fit is used to determine the stresses and strains. Because of the low thermal conductivity at low temperatures (see Fig. A.1), the temperature gradient of the solution is high for small values of x.

With A_s = 546.6 mm^2 the heat flow rate can be calculated from Eq. (A.6). This results in $\dot{Q}_x = -1.5$ W, where the minus sign indicates that heat flows in the negative x-direction.

The elastic properties of the laminate are determined by the elastic properties of the plies, their orientation, and their stacking sequence. The deformations of the laminate under thermal and mechanical loading are calculated using the assumptions of the classical theory of thin shells and plates:

- small deformations compared to material dimensions,
- linear–elastic material behaviour,
- plane sections remain plane,
- constant thickness and
- normals remain normals

and the assumptions of laminate theory:

- thin layers with homogeneous and orthotropic material behaviour,
- constant thickness of each layer and
- no displacement between adjacent layers [25].

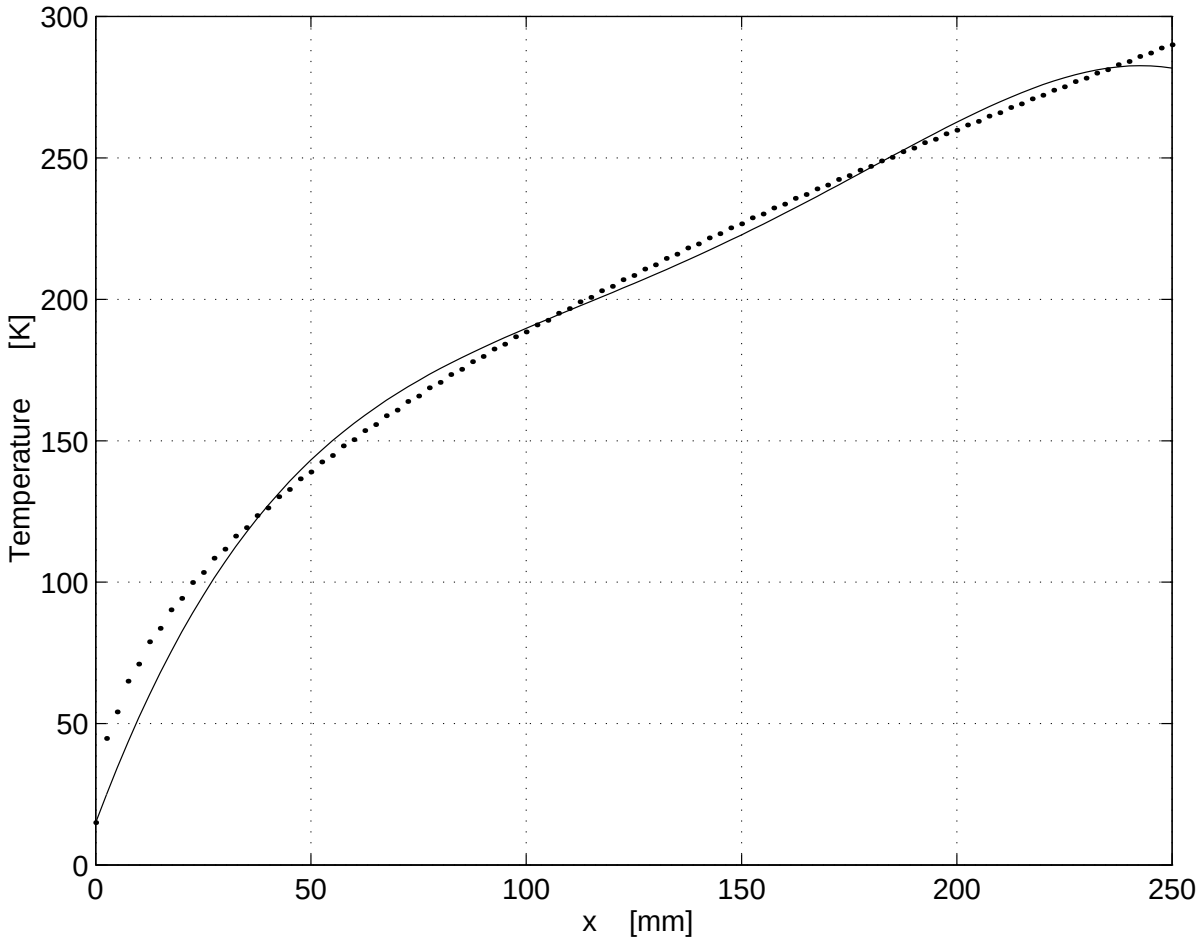

Figure 3.2: Temperature ϑ as a function of x. Solution of the differential equation of conduction of heat (dotted line) and fit to the solution (continuous line). Cold end at $x = 0$, warm end at $x = L = 250$ mm

As a result of these assumptions, displacements are linearly dependent on thickness. Out-of-plane sheer deformations are zero.

The deformation of the orthotropic laminate is calculated first and is used to determine the real strain of each single ply. The residual strains of each ply are calculated by subtracting the free thermal expansion strains from the real strains. Afterwards, the ply stresses are calculated from the residual strains, using the ply-stiffness matrices.

For the cylindrical orthotropic tube under the mechanical and thermal loading conditions as shown in Fig. 3.1, the following boundary conditions must hold:

$$\begin{aligned} N_x(L) &= F\,, \quad u(0,\theta) = 0\,, \\ M_x(0) &= 0\,, \quad N_\theta(0) = 0\,, \\ M_x(L) &= 0\,, \quad N_\theta(L) = 0\,, \end{aligned} \tag{3.4}$$

where N_i and M_i are defined in Eq. (B.1) and u is the displacement in the axial direction. The elastic properties, as well as the coefficients of thermal expansion of the laminate are assumed to be independent of temperature. The laminate itself is balanced and antisymmetric (four plies of equal thickness, stacking sequence $+\alpha/-\alpha/+\alpha/-\alpha$). Therefore, the elements A_{16} and A_{26} of the laminate's extensional stiffness matrix as well as the elements D_{16} and D_{26} of the lam-

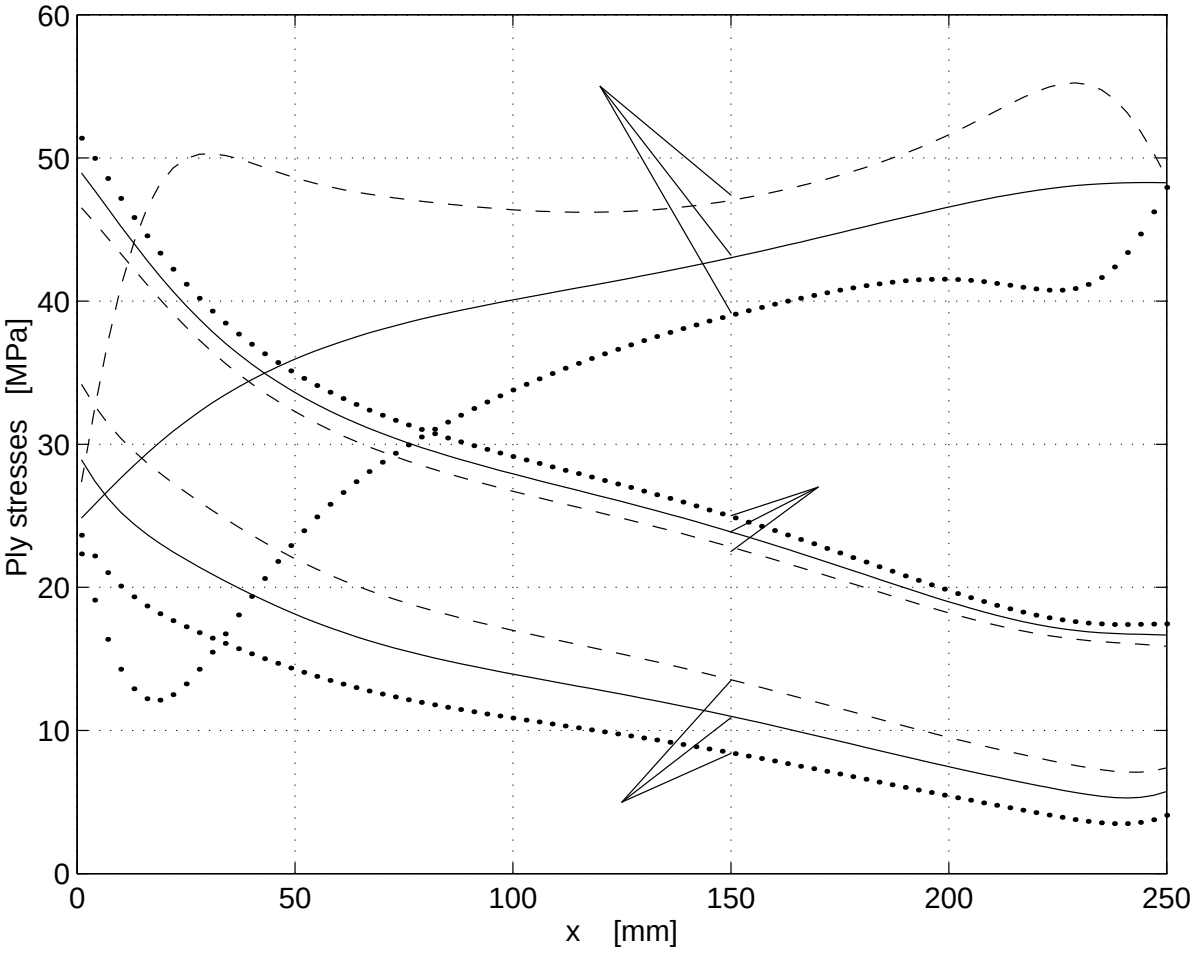

Figure 3.3: Ply stresses σ_1, σ_2, and τ_{12} as a function of x. Winding angle $\alpha = 18°$, cold end at $x = 0$, warm end at $x = L = 250$ mm

inate's bending stiffness matrix are zero [26]. Owing to the winding process, we assume that each layer itself is made up of a large number of thin layers, one layer with a positive angle towards the x-axis and one layer with a negative angle. Filament-wound laminates usually have this property. It can be shown [26] that for these laminates the coupling stiffness matrix vanishes ($B = 0$). This means curvatures do not lead to force resultants, and midplane strains do not lead to moment resultants. Furthermore, thermal loading causes neither shear forces nor shear moments. The loading and the geometry of the tube is symmetric with respect to the circumferential coordinate. Therefore the displacement in circumferential direction v equals zero, and $\partial(\ )/\partial\theta = 0$. In Appendix B, the equations are simplified using the above assumptions and solved for the boundary conditions given in Eq. (3.4).

The ply stresses and strains as a function of tube length are shown in Fig. 3.3. The stresses in the outer layer of the tube are represented by the dashed line, the stresses in the inner layer by a dotted line, and midplane stresses by a continuous line. We see that the thermal load causes considerable shear and transverse stresses for a cylindrical tube with a winding angle of 18°.

3.2 Failure Analysis

With the ply stresses known we can perform a ply failure analysis with the *Azzi–Tsai–Hill criterion* [1]. This criterion says that failure occurs from tensile loading of a ply when the following equation is satisfied for $S \leq 1$:

$$\frac{\sigma_1^2}{S_L^2} - \frac{\sigma_1 \sigma_2}{S_L^2} + \frac{\sigma_2^2}{S_T^2} + \frac{\tau_{12}^2}{S_S^2} = \frac{1}{S}\,, \tag{3.5}$$

where σ_1, σ_2, and τ_{12} are the ply stresses in the fibre direction, the transverse direction, and the in-plane shear stresses as calculated in Eq. (B.44) ($\sigma_1 = \sigma_1^p$, $\sigma_2 = \sigma_2^p$ and $\tau_{12} = \sigma_6^p$). The longitudinal tensile strength, the transverse tensile strength, and the in-plane (intra-laminar) shear strength of the ply are S_L, S_T, and S_S respectively (the strength values from the manufacturer are given in Section 2). The safety factor is S. It is plotted as a function of the winding angle for three different x-coordinates in Fig. 3.4.

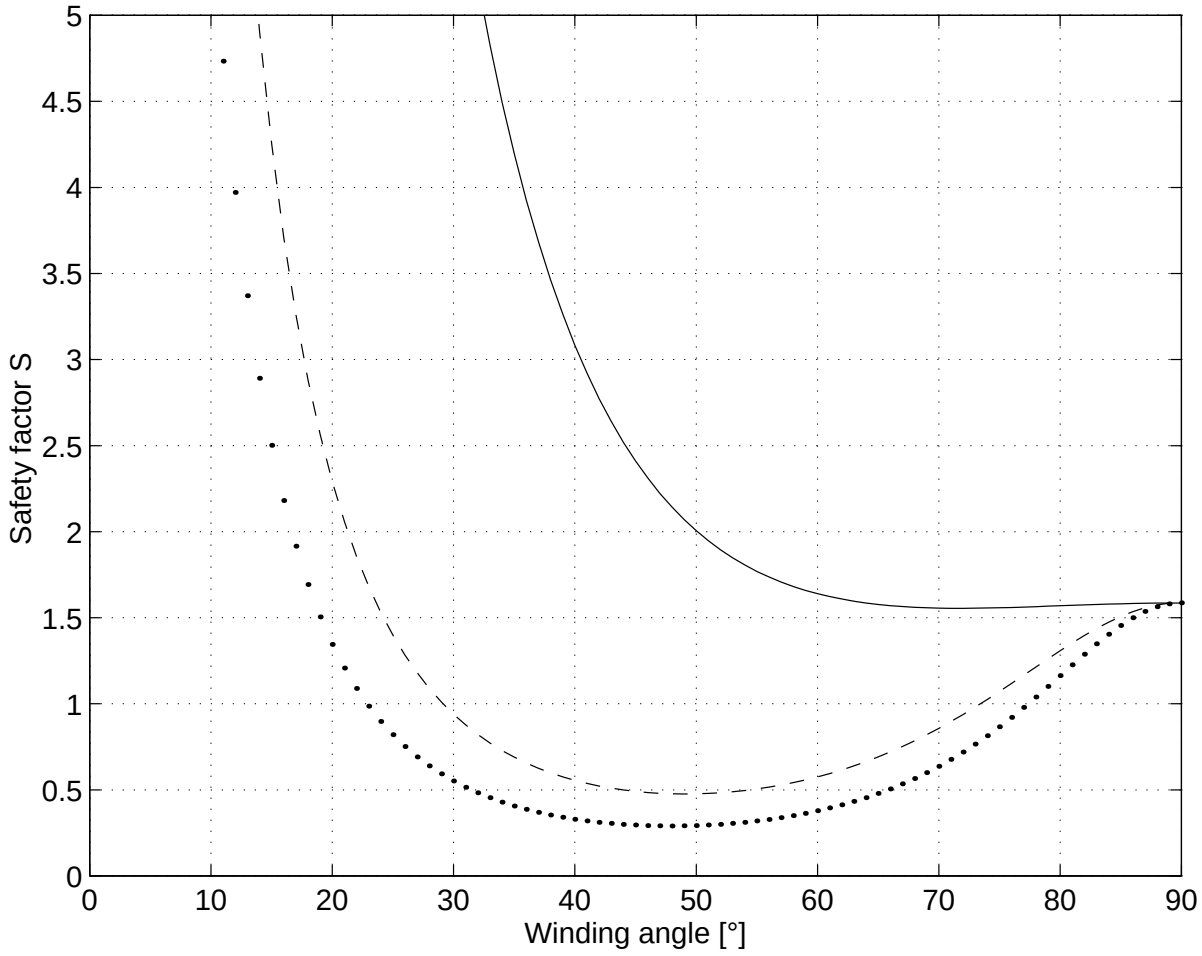

Figure 3.4: Safety factor S as a function of the winding angle at $x = 0$ (cold end, dotted line), at $x = 30$ mm (dashed line), and at $x = L = 250$ mm (warm end, continuous line)

We see that the safety factor decreases considerably towards the cold end of the tube. This is because of the low shear and transverse *strength* (Table 2.3) in combination with the high shear and transverse *stresses* (see Fig. 3.3). At 30 mm from the cold end (dashed line), considerably higher safety factors are obtained and even higher factors at the warm end (continuous line), where the thermal load is small. For 90°, the safety factors are about equal at all tube coordinates. There is no shear stress and the transverse strain is constant over the tube length. The stress in the circumferential direction is too small to lead to large variations of the safety factor (at 90° the fibres are aligned in the circumferential direction). It is interesting to see that, according to our model, the tube would fail at its cold end for winding angles α between 23° and 77°.

We should keep in mind the limits of our model. On the one hand, the thermal stresses and strains at the cold end of the tube are overestimated because we have considered constant coefficients of thermal expansion, while they actually approach zero with decreasing temperature. On the other hand these results do not consider the intra-laminar thermal stresses that are caused by the inhomogeneity of each single ply (each single ply is assumed to be homogeneous in laminate theory). No data are available from the manufacturer (Stesalit AG, Switzerland) on the dependence of elastic and thermal properties on temperature for cryogenic applications.

Not only the elastic and thermal constants, but also the strength of a ply vary with temperature. Reed et al. [5] state for structures spanning the interval from cryogenic to room temperatures that "... the strength of fibre-reinforced epoxy matrix composites usually increases at low temperature ...", and they continue,"...thus the weak link from the standpoint of *strength* is at room temperature". The above results show, however, that the thermal *stresses* at the cold end can be considerably higher than at the room temperature end of the structure. Therefore, it is a priori not clear whether the weak link is at cryogenic temperature or at room temperature. Mallick [1] states that "...significant curing stresses may develop owing to the thermal mismatch of various laminates. In some cases these stresses may be sufficiently high to cause intra-laminar cracks". We conclude from our model that thermal stresses are very important in our application and that testing under nominal mechanical and thermal conditions is necessary for further development. In this context it is interesting to quote Reed et al. [5] who state: "It is strongly recommended that additional fatigue tests be conducted ...".

The results presented in Fig. 3.4 indicate that decreasing the winding angle from 18° to 12°, for example, would considerably decrease the thermal stresses and hence increase the safety factor.

4 Tests and Results

Long duration **fatigue tests** were performed with two carbon-fibre tubes as described in Section 2. Nominal mechanical and thermal loads were applied. Three methods of non-destructive material evaluation were employed to detect possible defects such as matrix micro cracking, delamination, and fibre breakage in the laminate. Each evaluation method was applied once before and once after the fatigue test.

4.1 Test Set-up

The **test set-up** for the fatigue tests is shown in Fig. 4.1–4.3. A screw drive applies a static load to a steel tube which passes through the carbon-fibre tube to the upper flange of the spring package (see Fig. 4.2, bottom of assembly). The spring package, which is under compression, simulates the elasticity of the RF cavity. The lower plate is connected to the flange holding the cold end of the carbon-fibre tube. The dynamic load is given by a magnetostrictive actuator mounted in series with the screw drive and the steel tube. Its elongation results in a compressive force on the steel tube and a tensile force on the carbon-fibre tube.

A force transducer measures the tensile force in the carbon-fibre tube and an inductive transducer measures the displacement of the spring package. Both signals can be displayed on an oscilloscope.

For the tests with a temperature gradient across the carbon-fibre tube, the test assembly has been installed in a cryostat (see Fig. 4.1). The carbon-fibre tube, the steel tube, and the two metal plates are located inside the cryostat. One end of the carbon-fibre tube was at liquid helium temperature the other end at room temperature.

Figure 4.1: Test set-up with cryostat, power amplifier and control instrumentation

Figure 4.2: Test set-up at room temperature

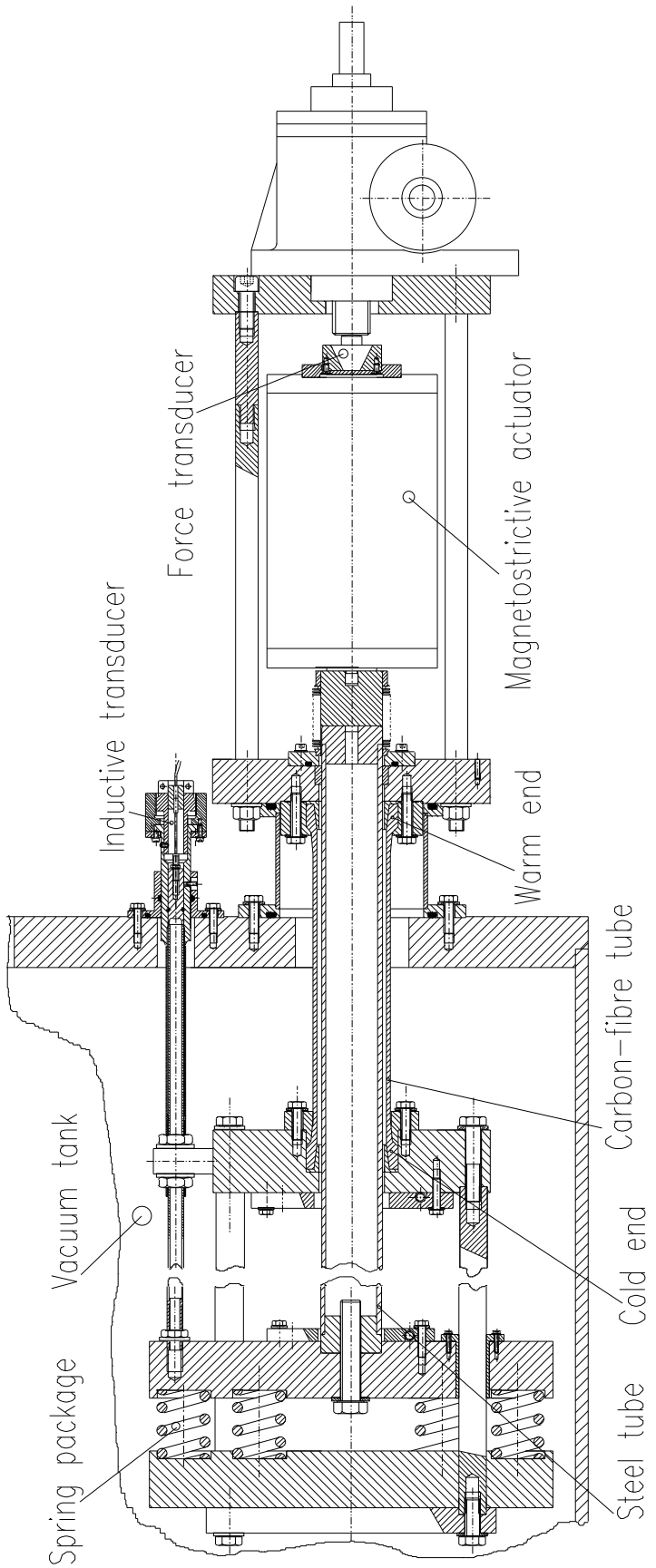

Figure 4.3: Test assembly

4.2 Tests

Both tubes were subjected to a static tensile load of 27 kN and to a dynamic load of 1 kN with varying frequency (10–20 Hz) (see Table 4.1). Higher test frequencies could be obtained,

Table 4.1: Summary of the fatigue tests of the two tubes

	Tube 1	Tube 2
Number of cycles (warm test)	25 400 000	3 500 000
Frequency [Hz]	20	15
Dynamic load [kN]	1	1
Number of cycles (cold test)	3 500 000	3 800 000
Frequency [Hz]	10–15	15
Dynamic load [kN]	1	1

but only at the expense of smaller force amplitudes. While a relatively high number of cycles were possible at room temperature, cycling at cryogenic temperatures was limited by the cost of helium: 500 litres of helium lasted for about 8 hours. Cooling was interrupted overnight while the mechanical load continued on the tubes. Thus, some thermal cycling was achieved.

Figure 4.4 shows the signal of the inductive transducer (see Fig. 4.3) together with the signal of the current probe. The compression of the spring package is about 100 μm when the magnetostrictive actuator is driven by a current of 85 A. The frequency is 15 Hz. Both tubes withstood the load summarized in Table 4.1 without any visible damage.

Figure 4.4: Actuator current (upper trace, 20 A/div) and compression of the spring package (lower trace, 20 μm/div). Time scale: 10 ms/div

4.3 Material Inspection

From many methods that are used for non-destructive material inspection such as radiography, thermography, and acoustic-emission testing [27]–[29], we chose the following three to examine the tubes (see Fig. 4.5):

- Measurement of the tube geometry
- Microscopy of the side faces
- Ultrasonic inspection

.

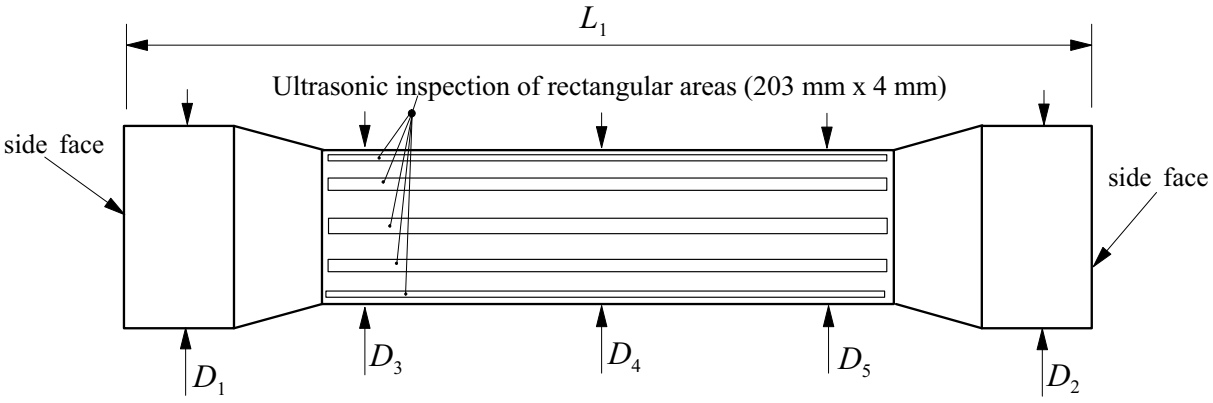

Figure 4.5: Location of ultrasonic inspection areas and geometry measurements (L_1, and D_1 to D_5)

4.3.1 Measurement of the Tube Geometry

A *Ferranti MERLIN* 750 three-dimensional computer-supported measurement system with a resolution of ± 3 μm was used to measure the dimensions of the tube before and after the fatigue tests in order to detect possible plastic deformations due to internal defects such as fibre breakage or delaminations. The diameters D_1 and D_2 (see Fig. 4.5) could also change, if the attachment of glass fleece on the carbon-fibre cone in the end sections were to fail.

To measure the flatness of the tube's side faces, eight coordinates of each side face were measured and a plane was fitted to the eight points. In a similar way, the diameters of the machined surfaces (D_1, D_2) at both end sections were recorded by fitting a circle to eight measured coordinates on the circumference. The length of the tube (L_1) could now be calculated as the distance between the two side faces along a straight line through the centre of the two circles. This line was defined as the axis of the tube. Furthermore, the diameter of the unmachined cylindrical part of the tube was measured at three axial coordinates (D_3, D_4, D_5, see Fig. 4.5). The results are listed in Table 4.2.

Table 4.2: Measurements of the tube geometry, see also Fig. 4.5; (all values in mm)

	Before	After	Difference
Tube length (L_1)	290.174	290.176	$+0.002$
Diameter of machined end section (D_1)	72.869	72.863	-0.006
Diameter of machined end section (D_2)	72.860	72.869	$+0.009$
Diameter of cylindrical part (D_3)	60.961	60.955	-0.006
Diameter of cylindrical part (D_4)	60.760	60.760	0.000
Diameter of cylindrical part (D_5)	60.725	60.716	-0.009

The differences lie between $+9$ μm and -9 μm. They are possibly caused by:

1. The resolution of the system is ± 3 μm which could add up to 6 μm.

2. The room temperature was kept in the range 20 ± 0.5°C. Therefore, the tube temperature could have been different by up to 1°C between the two measurements. Warming up the tube by 1°C increases the diameter of the machined end sections by about 2.5 μm and decreases the tube length by about 0.2 μm.

3. The tube was positioned on a V-shaped support. Although eight coordinates were measured to minimize statistical errors, some deviations due to positioning tolerances cannot be excluded.

We conclude that the differences (Table 4.2) are too small to indicate substantial delaminations or fibre breakage. Any plastic deformation of the end sections with the difficult bonding of the glass fleece to the carbon-fibre cone (see Fig. 2.3) could not be seen.

4.3.2 Microscopy of the Side Faces

The side faces of the tube were polished with a soft felt. Pictures were taken at three points on each side face with different magnifications before and after the fatigue tests.

On all pictures (Fig. 4.6–4.13), big holes (black) can be seen as islands in the surrounding fibre–matrix mixture (fibres white, matrix grey). The glass fleece appears with a medium grey colour.

Comparing the pairs of corresponding pictures, one can see that the overall geometry of holes and surrounding fibre–matrix mixture has not changed. In most cases each single fibre can be recognized. No cracks or fibre pull-out can be seen and the bonding between the fibre–matrix layer and the glass fleece layer is unchanged.

The pictures taken after the fatigue tests are not as clear as those taken before. Little arc-shaped scratches diminish their quality. Fine traces of carbon on the V-shaped support indicate that the scratches were caused when the tube was turned on the V-shaped support during the ultrasonic examination.

Figure 4.6: Microscopic picture of the cold end section of the tube, **before** fatigue test, magnification $\times$ 100

Figure 4.7: Microscopic picture of the cold end section of the tube, **before** fatigue test, magnification $\times$ 550

Figure 4.8: Microscopic picture of the cold end section of the tube, **after** fatigue test, magnification $\times$ 100

Figure 4.9: Microscopic picture of the cold end section of the tube, **after** fatigue test, magnification $\times$ 550

Figure 4.10: Microscopic picture of the warm end section of the tube, **before** fatigue test, magnification $\times$ 100

Figure 4.11: Microscopic picture of the warm end section of the tube, **before** fatigue test, magnification $\times$ 550

Figure 4.12: Microscopic picture of the warm end section of the tube, **after** fatigue test, magnification $\times$ 100

Figure 4.13: Microscopic picture of the warm end section of the tube, **after** fatigue test, magnification $\times$ 550

4.3.3 Ultrasonic Inspection

In ultrasonic inspection, sound waves are used to detect internal defects in a probe. The sound waves are produced by electrically exciting a piezoelectric transducer; they then enter the probe via a liquid coupling medium. Inside the probe, the sound waves are reflected and/or attenuated by internal defects. The reflected and the transmitted sound waves can be converted into electrical signals by means of receiving transducers.

In the **through-transmission method**, the piezoelectric receiver is positioned at the back surface of the material. It receives the sound waves from the sending transducer at the front surface of the material. At a location of a defect the received signal is weaker than at other locations. The received signals are compared with preset threshold values and displayed. It is obvious that the through-transmission method requires access to the back surface of the probe. For our tube access to the back surface is difficult.

We use the **impulse-echo method**. Here, the reflected sound waves are picked up either by the sending transducer itself or by a second receiving transducer close by. The signals are sent to a cathode-ray tube screen, where their amplitudes are plotted versus time. This is a so-called **A-scan** (see Fig. 4.14). A typical A-scan of homogeneous test material without any defects is a horizontal line with two peaks. The first peak is caused by the reflection on the front surface of the probe, and the second peak is caused by its back surface. The distance between the two peaks on the horizontal axis is proportional to the time it took the sound waves to travel twice through the probe (see Fig. 4.14). In the case of internal defects or inhomogeneities further reflections occur. Their location (deepness) in the material can be calculated from the distance between the different peaks and the velocity of sound in the probe.

Figure 4.14: Ultrasonic testing with the impulse-echo method and an A-scan [1]

A **C-scan** is a plane view representation of the probe. It consists of a two-dimensional array of measurement points. Each measurement point corresponds to one position of the sending transducer. The magnitude of echoes caused either by defects (**interface echo**) or by the back surface of the probe (**back surface echo**) is, for each measurement point, represented by a colour or grey scale. The back surface echo is weak when the interface echo is strong, and vice versa. Consequently, two C-scans of the same probe, one showing the interface echo, the other one showing the back surface echo, have inverted colours or grey scales.

Ultrasonic inspection of fibre-reinforced laminates is more difficult than for metals. The laminates are by nature inhomogeneous and anisotropic (fibre and matrix) and they often have air inclusions due to the manufacturing process (they can be clearly seen in our microscopic pictures of the side faces). As a result, a scan of an undamaged laminate shows echo amplitudes

which vary much more strongly than in a scan of an undamaged metal. It is therefore a priori not clear how to detect a defect in a laminate.

However, ultrasonic inspection has been successfully used by other experimenters. For example, Henneke [30] reports on experiments with graphite-fibre-reinforced epoxy laminates before and after fatigue loading. He found clear indications of damage propagation (increasing number of cracks and growing delaminations). Hillger [31] investigated the resolution of C-scans using an 80 μm thin Teflon film as artificial delamination in the midplane of a 4 mm thick laminate. He showed that delaminations with diameters as small as 300 μm can be detected.

The tubes were examined using two different ultrasonic inspection systems: A *Krautkrämer USIP* 12 system which is mainly for the examination of flat probes and a *USL (Ultrasonic Sciences Ltd)* system which also allows curved probes to be scanned in one turn by rotating them automatically on a turntable with a stepping motor. This minimizes errors due to bad alignment. To use the *Krautkrämer* system for our tubes, a V-shaped support structure was constructed allowing several long thin areas to be scanned by rotating the tube manually after each scan (see Fig. 4.5).

Scan	No. 1	No. 2	No. 3	No. 4	No. 5
Compression cycles	0	1	2	3	4
Applied load (kN)	0	100	130	97	99
Cracking sound	No	No	Yes	Yes	Yes
C-scans					

Figure 4.15: Detection of defects caused by compression

Detection of Defects We investigated the problem of defect detection and compared C-scans of an undamaged laminate with C-scans of the same laminate after it was exposed to increasing mechanical load cycles until damage occurred (Fig. 4.15).

Figure 4.16 shows the colour palette. The white colour corresponds to a no or a low echo amplitude, the black colour corresponds to a strong echo amplitude. Strong echo amplitudes

Figure 4.16: The colour palette for different echo amplitudes

are caused by internal defects and inhomogeneities. Consequently, using interface echo, defects dark-shift the colour of a C-scan. Figure 4.15 shows five C-scans of the same area of one sample tube. After a preliminary scan the tube was exposed to one load cycle. An axial compressive load of 100 kN was applied to the tube sample which has a 400 mm^2 cross-section. After this first load cycle the tube sample was examined by ultrasonic inspection again. Then the load was successively increased until the sound of fibre breakage was heard. The test was then immediately stopped and the tube was scanned again. Following this scheme four compression cycles were performed and five C-scans recorded.

We can see in Fig. 4.15 that no substantial changes occurred during the first three load cycles. The last compression cycle, however, caused a defect which can be seen as a black area in the lower half of scan no. 5 (marked ”*“). The lower part of scan no. 5 differs completely from the corresponding parts of scans no. 1–4. The colour shifts from light blue and yellow to black which corresponds to 5–6 steps of the colour palette. Also the shape of the damaged area of scan no. 5 is very different from the corresponding areas of scans no. 1–4. We are sure of having looked at the same area of the sample since other patterns of the scanned area repeat themselves from scan no. 1 to scan no. 5, for example, the large dark spot on the top.

The defect on scan no. 5 (marked ”*“) can also be seen in a complementary A-scan (Fig. 4.17). It shows the echo peaks of the front surface (left peak), the back surface (right peak) and in between the echo caused by an internal defect.

Figure 4.17: Ultrasonic A-scan of the defect area of scan no. 5 in Fig. 4.15 (marked ”*“)

Area 1		Area 2		Area 3	
Scan 1	Scan 2	Scan 1	Scan 2	Scan 1	Scan 2

Figure 4.18: Repeatability test

Repeatability Test To investigate the accuracy of alignment of the carbon tube on the V-shaped support, two scans of three areas (203 mm $\times$ 4 mm) were performed. Between the two scans the tube was taken from the V-shaped support and realigned using an optical mark.

Figure 4.18 shows the results. In the case of perfect repeatability two pictures of the same area should be identical. However, some deviations can be observed but colour variations in most cases do not exceed one colour step in the palette (Fig. 4.16). The size and the shape of patterns of equal colour change only slightly but most patterns such as points or long shapes can easily be recognized. No strong deviations (such as the one due to damage between scan no. 4 and scan no. 5 in Fig. 4.15) can be seen.

Area 1		Area 2		Area 3	
Before	After	Before	After	Before	After

Figure 4.19: C-scans before and after the fatigue tests

Ultrasonic Investigation of Tube We scanned 12 thin rectangular areas (see Fig. 4.5), each of them once before and once after the fatigue tests. Three pairs of typical C-scans out of 12 are presented in Fig. 4.19. Slight variations in colour and shape of the recorded patterns can be seen. Most changes in colour do not exceed one step in the colour palette (for example from green to red), and most patterns change shape only slightly. Substantial changes, however, such as caused by our compression test (see scan no. 4 and scan no. 5 in Fig. 4.15), are not observed. The differences between two C-scans of the same area (Fig. 4.19) are no bigger than the differences found in the previous repeatability tests (Fig. 4.18).

Two pairs of C-scans of the whole tube were recorded. Figures 4.20 and 4.21 show the back surface echo, whereas Figs. 4.22 and 4.23 show the interface echo. The whole surface C-scans (Figs. 4.20–4.23) confirm the results of the partial scans (of the long thin areas) presented above. The inhomogeneities which are due to the manufacturing process can be clearly seen. Moreover, the whole surface C-scans show that these inhomogeneities have regularities which could not be observed from the narrow partial scans: line patterns of equal colour are running along the C-scans with constant slopes. They correspond to the winding angle of the tube of 18°. In general, all patterns repeat themselves better in the whole surface scan than in the partial scans. Hardly any difference can be found between Fig. 4.20 and Fig. 4.21. This is most likely due to the smaller alignment errors. From the high similarity of corresponding C-scans which were taken before and after the fatigue test with both ultrasonic inspection systems, we conclude that no defects (such as those caused by our compression tests) were caused by the fatigue tests.

Figure 4.20: Ultrasonic C-scan of the cylindrical part of the tube **before** the fatigue tests, using the echo of the back surface (B); transducer: 2.25 MHz; focal length: 64 mm

Figure 4.21: Ultrasonic C-scan of the cylindrical part of the tube **after** the fatigue tests, using the echo of the back surface (B); transducer: 2.25 MHz; focal length: 64 mm

Figure 4.22: Ultrasonic C-scan of the cylindrical part of the tube **before** the fatigue tests, using interface echo (between A and B); transducer: 5 MHz; focal length: 32 mm

Figure 4.23: Ultrasonic C-scan of the cylindrical part of the tube **after** the fatigue tests, using interface echo (between A and B); transducer: 5 MHz; focal length: 32 mm

5 Conclusions

The carbon-fibre tube of the tuning structure of the superconducting RF cavities of the LHC has to satisfy conflicting requirements: high mechanical stiffness and low thermal conduction. In addition, the tube has to withstand the oscillatory tuning forces for a high number of loading cycles without fatigue failure.

We have designed a tube of carbon-fibre-reinforced laminate which meets these requirements. Two tubes have been successfully manufactured and tested under nominal mechanical and thermal loads. After a large number of loading cycles (up to 28 million) no signs of material fatigue could be detected by precise geometry measurements, microscopy, and extensive ultrasonic inspection.

We have demonstrated that ultrasonic inspection is a good tool to look for defects in carbon-fibre-reinforced laminates. Good repeatability was obtained and damage caused by cyclic compression loading was easily detected.
For further developments we recommend:

- Reduction of the winding angle. This will increase the axial stiffness at the expense of reduced radial strength which is acceptable.
- Stress due to thermal gradients can be important as shown by model calculations. The fatigue due to a large number of thermal cycles should be investigated.
- Radiation can cause considerable loss of strength of the matrix, in particular when the matrix is prestressed. Since the tube is under permanent tensile stress additional irradiation tests are recommended.

Acknowledgements

We would like to express our gratitude to:

D. Boussard and G. Passardi, who supported the project; C. Hauviller and M. Mathieu for helping with material and for fruitful discussions; M. Kubly, F. Gusti and B. Girod for preparing tube samples; J.-P. Bacher, S. Sgobba, and H. Fritz for their support when performing the tests, in particular during the ultrasonic inspection; J.-L. Escourrou for setting up and operating the cryogenic test assembly; D. Stellfeld for the installation and operation of the test, X. Lagrue and C. Ruivet for designing the test assembly; Prof. Hartwig (Forschungszentrum Karlsruhe) for many fruitful discussions and new ideas; J. Neuenschwander (EMPA Zürich) for performing ultrasonic inspections; Mr. Voirol and Mr. Stich (Stesalit AG in Zulwill (Switzerland)) for manufacture of the tube.

References

[1] P.K. Mallick, *Fiber-Reinforced Composites, Materials, Manufacturing, and Design* (Marcel Dekker, New York, 1993).

[2] The LHC Study Group, *LHC — The Large Hadron Collider, Conceptual Design*, CERN/AC/95–05 (CERN, Geneva, 1995).

[3] M. Blin et al., *Design, Construction and Performance of Superconducting Magnet Support Posts for the Large Hadron Collider*, LHC Project Note 235 (CERN, Geneva, 1993).

[4] M. Karmarkar and V. Rödel, *Considerations on a Tuning System for the LHC Superconducting RF Cavity*, SL/Note 93–105 (RFS) (CERN, Geneva, 1993).

[5] R.P. Reed and M. Golda, Cryogenic Properties of Unidirectional Composites, in *Cryogenics, Vol. 34, Nr. 11, pp. 909–928* (1994).

[6] G. Hartwig and K. Pannkoke, Fatigue Behaviour of UD-Carbon-Fiber Composites at Cryogenic Temperatures, in *Adv. Cryo. Eng. Mater., Vol. 38, pp. 453–457* (1994).

[7] G. Hartwig and R. Hübner, Thermal and Fatigue Cycling on Fibre Composites, in *Cryogenics, Vol. 35, pp. 727–730* (1995).

[8] A.F. Clark, R.P. Reed and G. Hartwig, *Nonmetallic Materials and Composites at Low Temperatures* (Plenum, New York, 1979).

[9] J. Genest, *Calculs Mechanique d'une Cavite Monocellule Supraconductrice pour le LHC*, Note Technique MT-ES/91–21 (CERN, Geneva, 1994).

[10] M. Huhtinen and G.R. Stevenson, *Doses around the LHC beam–pipe due to beam–gas interactions in a long straight section*, LHC Project Note 39 (CERN, Geneva, 1996).

[11] G. Passardi, *private communication* (1993).

[12] W. Beitz et al., *H. Dubbel, Taschenbuch für den Maschinenbau, 17. Auflage* (Springer, Berlin, 1990).

[13] M. Tavlet, *Radiation Resistance of Carbon/Epoxy Composite Material*, TIS Report R 552 (CERN, Geneva, 1994).

[14] S.G. Burnay, Effect of Pre-Stressing on the Behaviour of CFRP under Gamma Irradiation, in *ESA Journal, Vol. 16, pp. 435–445* (1992).

[15] G. Lindenberger, M. St ich and P. Voirol, *Stesalit AG, Switzerland, private communication* (1996–97).

[16] M.W. Hyer, Stresses and Deformations in Composite Tubes Due to a Circumferential Temperature Gradient, in *J. Appl. Mech., Vol. 53, pp. 757–764* (1986).

[17] M.W. Hyer, Thermally Induced Stresses and Deformations in Angle-Ply Composite Tubes, in *J. Compos. Mater., Vol. 21, pp. 455–480* (1987).

[18] R. Jakobi, *Zur Spannungs-, Verformungs- und Bruchanalyse an dickwandigen, rohrförmigen Bauteilen aus Faser-Kunststoff-Verbunden* (VDI Verlag, Reihe 5, 126, Düsseldorf, 1987).

[19] J.A. Nairn, Thermoelastic Analysis of Residual Stresses in Unidirectional, High-Performance Composites, in *Polymer Compos., Vol. 6, 2, pp. 123–130* (1985).

[20] J.M. Whitney, A Refined Theory for Laminated Anisotropic, Cylindrical Shells, in *Trans. ASME, J. Appl. Mech., series E/41, pp. 471–476* (1974).

[21] J.M. Whitney, On the Use of Shell Theory for Determining Stresses in Composite Cylinders, in *J. of Compos. Mater., Vol. 5, pp. 340–353* (1971).

[22] W. Haben, *Analytische Verfahren zur Berechnung orthotroper Faserverbund-Zylinderschalen, (Diplomarbeit)* (Technische Universität Clausthal, Germany, 1990).

[23] B.W. Smith et al., Failure Analysis of Continuous-Fibre-Reinforced Composites, in *ASM Handbook, Vol. 11, 10th Edition, Failure Analysis and Prevention, pp. 731–743* (ASM, Metals Park, Ohio, 1995).

[24] H.S. Carlslaw, *Conduction of Heat in Solids, 2nd ed* (Oxford University Press 1992).

[25] A.S. Herrmann, *Mechanik der Faserverbundwerkstoffe I, (Vorlesungsumdruck)* (Technische Universität Clausthal, Germany, 1996).

[26] R.M. Jones, *Mechanics of Composite Materials* (Scripta Book Company, 1975).

[27] ASM Handbook, *Nondestructive Evaluation and Quality Control, Vol. 17, 10th ed* (ASM International, USA, 1996).

[28] J. Summerscales, editor, *Non-Destructive Testing of Fibre-Reinforced-Plastics Composites, Vol. 1* (Elsevier, New York, 1987).

[29] J. Summerscales, editor, *Non-Destructive Testing of Fibre-Reinforced-Plastics Composites, Vol. 2* (Elsevier, New York, 1990).

[30] E.G. Henneke, Ultrasonic Nondestructive Evaluation of Advanced Composites, in *Non-Destructive Testing of Fibre-Reinforced Composites, Vol. 2, pp. 55–160, J. Summerscales, editor* (Elsevier, New York, 1990).

[31] W. Hillger et al., Ultraschallprüfung an Faserverbundkunststoffen, Grundlagen, Methoden der bildhaften Darstellung und Ergebnisse, in *Material-Wissenschaften und Werkstofftechnik, Vol. 22, pp. 217–224* (1991).

[32] M. Mathieu, *private communication* (1997).

[33] W. Flügge, *Stresses in Shells, 2nd ed* (Springer, Berlin, 1973).

[34] Il'ja N. Bronštein, *Taschenbuch der Mathematik* (Verlag Harri Deutsch, Thun, 1989).

Appendix A: Temperature Distribution

We use Eq. (3.2) from Section 3

$$\frac{\mathrm{d}}{\mathrm{d}x}\left(\lambda_3(\vartheta)\frac{\mathrm{d}\vartheta}{\mathrm{d}x}\right) = 0\ , \tag{A.1}$$

where the temperature dependence of the thermal conductivity is given by

$$\lambda_3(\vartheta) = a_\lambda\vartheta^3 + b_\lambda\vartheta^2 + c_\lambda\vartheta + d_\lambda\ . \tag{A.2}$$

The constants a_λ, b_λ, c_λ, and d_λ are determined by a least-square fit to extrapolated experimental data (see Fig. A.1):

$$\begin{aligned} a_\lambda &= -1.64\times10^{-7}\ \mathrm{W/(m\cdot K^4)}\ , \\ b_\lambda &= 6.50\times10^{-5}\ \mathrm{W/(m\cdot K^3)}\ , \\ c_\lambda &= 1.25\times10^{-2}\ \mathrm{W/(m\cdot K^2)}\ , \\ d_\lambda &= -1.39\times10^{-1}\ \mathrm{W/(m\cdot K)}\ . \end{aligned} \tag{A.3}$$

Integration of Eq. (3.2) gives

$$\lambda_3(\vartheta)\frac{\mathrm{d}\vartheta}{\mathrm{d}x} = \dot{q_x}\ , \tag{A.4}$$

where $\dot{q_x}$ is the heat flow rate per unit area in axial direction which is a constant.
Separating the variables and integrating we obtain the temperature as a function of the axial coordinate:

$$\int_{\vartheta_1}^{\vartheta}\lambda_3(\xi)\,\mathrm{d}\xi = \dot{q_x}\,x\ . \tag{A.5}$$

Integrating over the whole tube length we obtain for the heat flow rate

$$\dot{Q_x} = \dot{q_x}A_s = \int_{\vartheta_1}^{\vartheta_2}\lambda_3(\xi)\,\mathrm{d}\xi\,\frac{A_s}{L}\ . \tag{A.6}$$

Numerically solving Eq. (A.5) with $\vartheta_1 = 15$ K, $\vartheta_2 = 290$ K, A_s = 546.6 mm^2, and $L = 250$ mm, one obtains the temperature as a function of the axial coordinate x (see Fig. 3.2).
The heat flow resulting from Eq. (A.6) is $\dot{Q_x} = -1.5$ W. The negative sign indicates that heat flows in negative x-direction.
The fourth-order polynomial

$$\vartheta(x) = a_\vartheta x^4 + b_\vartheta x^3 + c_\vartheta x^2 + d_\vartheta x + e_\vartheta\ , \tag{A.7}$$

with

$$\begin{aligned} a_\vartheta &= -318334.1\ \mathrm{K/m^4}\ , \\ b_\vartheta &= 186248.4\ \mathrm{K/m^3}\ , \\ c_\vartheta &= 38687.9\ \mathrm{K/m^2}\ , \\ d_\vartheta &= 4072.4\ \mathrm{K/m}\ , \\ e_\vartheta &= \vartheta_1 = 15\ \mathrm{K}\ . \end{aligned} \tag{A.8}$$

was fitted to the numerical solution. Figure 3.2 in Section 3 shows the numerical solution (dotted line) and the curve fit (continuous line). Equation (A.7) is used in the following section to calculate the stress–strain distribution of the laminate.
Matlab software was used for the numerical solution of the differential equation of conduction of heat and for the curve fits. The program codes are listed below in Appendix C.

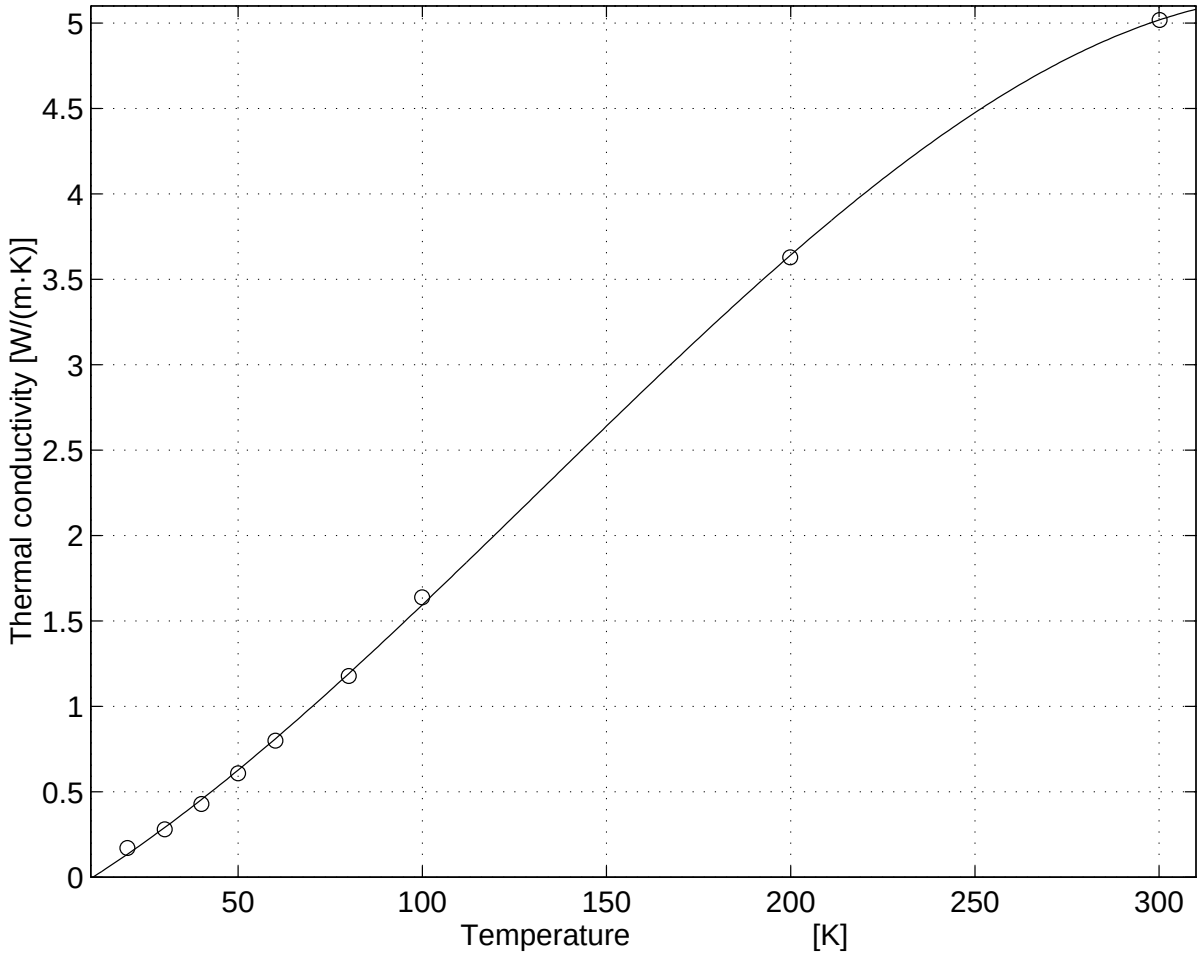

Figure A.1: Thermal conductivity as a function of temperature, least-square fit and extrapolated experimental data. The manufacturer (Stesalit AG) could only provide the value of thermal conductivity at room temperature. All other values were extrapolated using the measurements performed at CERN by M. Mathieu [32].

Appendix B: Ply Stresses and Strains

The forces and moment resultants[1] N_i, and M_i, are linked with the midplane strains and the shell curvatures, ϵ_i^0 and κ_i, respectively, by the following equations:

$$\left.\begin{array}{l} N_i = A_{ij}\epsilon_j^0 + B_{ij}\kappa_j - N_i^\vartheta \\ M_i = B_{ij}\epsilon_j^0 + D_{ij}\kappa_j - M_i^\vartheta \end{array}\right\} \; i,j = 1,2,6 \; , \tag{B.1}$$

where[2]

$$\left.\begin{array}{l} N_i = \int_{-h/2}^{h/2} \sigma_i \, \mathrm{d}z, \\ M_i = \int_{-h/2}^{h/2} \sigma_i \, z \, \mathrm{d}z \end{array}\right\} \; i = 1,2,6 \; , \tag{B.2}$$

with $(\;)_1 = (\;)_x$, $(\;)_2 = (\;)_\theta$, and $(\;)_6 = (\;)_{x\theta}$. The elements of the stiffness matrix can be written as

$$\left.\begin{array}{l} A_{ij} = \int_{-h/2}^{h/2} Q_{ij} \, \mathrm{d}z \\ B_{ij} = \int_{-h/2}^{h/2} Q_{ij} \, z \, \mathrm{d}z \\ D_{ij} = \int_{-h/2}^{h/2} Q_{ij} \, z^2 \, \mathrm{d}z \end{array}\right\} \; i,j = 1,2,6 \; , \tag{B.3}$$

and the thermal forces and moments can be expressed

$$\left.\begin{array}{l} N_i^\vartheta = \int_{-h/2}^{h/2} Q_{ij} \, \epsilon_j^\vartheta \, \mathrm{d}z \\ M_i^\vartheta = \int_{-h/2}^{h/2} Q_{ij} \, \epsilon_j^\vartheta \, z \, \mathrm{d}z \end{array}\right\} \; i,j = 1,2,6 \; , \tag{B.4}$$

where

$$\epsilon_i^\vartheta = \alpha_i \triangle \vartheta; \quad i = 1,2,6 \; , \tag{B.5}$$

and α_i are the coefficients of thermal expansion.
In Eqs. (B.3),(B.4), Q is the reduced anisotropic stiffness matrix for plane stress which has to be calculated for each ply. It relates ply stresses to ply strains in the coordinate system of the tube (x, θ, z-system), according to

$$\sigma_i = Q_{ij}(\epsilon_j - \epsilon_j^\vartheta); \quad i = 1,2,6 \; . \tag{B.6}$$

The matrix Q can be obtained from the ply-stiffness matrix in the ply-coordinate system (superscript p) which is

$$Q^p = \begin{pmatrix} Q_{11}^p & Q_{12}^p & Q_{16}^p \\ Q_{12}^p & Q_{22}^p & Q_{26}^p \\ Q_{16}^p & Q_{26}^p & Q_{66}^p \end{pmatrix} = \begin{pmatrix} \frac{E_{11}}{1-\nu_{12}\nu_{21}} & \frac{\nu_{12}E_{22}}{1-\nu_{12}\nu_{21}} & 0 \\ \frac{\nu_{12}E_{22}}{1-\nu_{12}\nu_{21}} & \frac{E_{22}}{1-\nu_{12}\nu_{21}} & 0 \\ 0 & 0 & G_{12} \end{pmatrix}, \tag{B.7}$$

where E_{11} is the elastic modulus of the ply in the fibre direction, E_{22} is the elastic modulus of one ply in the transverse direction, ν_{12} is the major Poisson ratio, ν_{21} is the minor Poisson ratio and G_{12} is the shear modulus of the ply.

[1] The units of N_i and M_i are not force and moment units, but force and moment divided by length. However, they are usually referred to as forces and moments, since they represent the forces divided by the width (or the circumference) of the laminate.

[2] Assuming $\frac{h}{2} << R$.

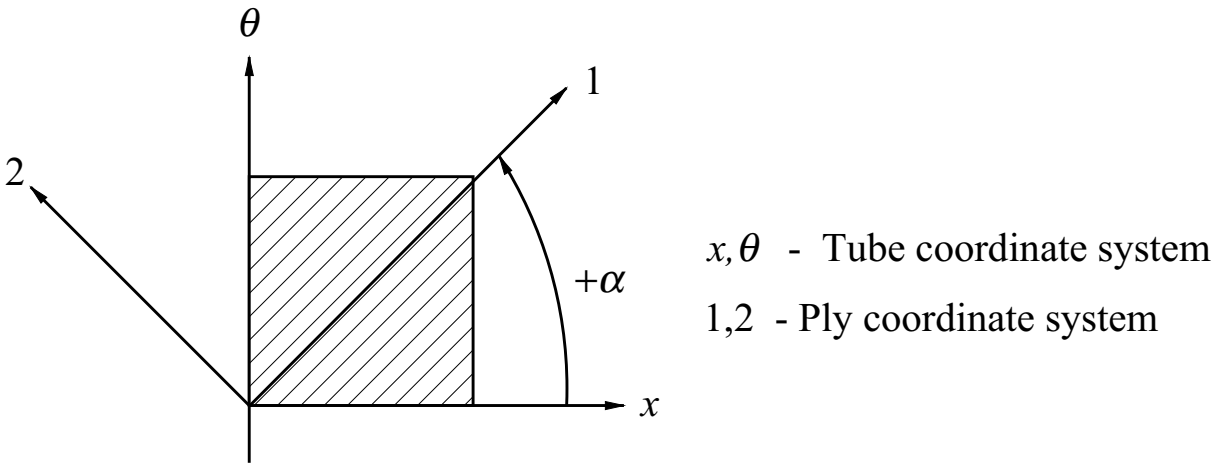

Figure B.1: Rotation from ply to global coordinate system

We obtain the reduced anisotropic stiffness matrix Q (for the tube coordinate system) from the reduced orthotropic stiffness matrix Q^p (for the ply-coordinate system) by means of a transformation[3] [26],[1] using the relation

$$Q = T_Q \, Q^p, \tag{B.8}$$

where

$$Q = \begin{pmatrix} Q_{11} \\ Q_{12} \\ Q_{22} \\ Q_{16} \\ Q_{26} \\ Q_{66} \end{pmatrix} \quad Q^p \begin{pmatrix} Q^p_{11} \\ Q^p_{12} \\ Q^p_{22} \\ Q^p_{16} \\ Q^p_{26} \\ Q^p_{66} \end{pmatrix} \tag{B.9}$$

and

$$T_Q = \begin{bmatrix} \mathrm{c}^4 & 2\mathrm{s}^2\mathrm{c}^2 & \mathrm{s}^4 & 0 & 0 & 4\mathrm{s}^2\mathrm{c}^2 \\ \mathrm{s}^2\mathrm{c}^2 & \mathrm{s}^4 + \mathrm{c}^4 & \mathrm{s}^2\mathrm{c}^2 & 0 & 0 & -4\mathrm{s}^2\mathrm{c}^2 \\ \mathrm{s}^4 & 2\mathrm{s}^2\mathrm{c}^2 & \mathrm{c}^4 & 0 & 0 & 4\mathrm{s}^2\mathrm{c}^2 \\ \mathrm{c}^3\mathrm{s} & \mathrm{s}^3\mathrm{c} - \mathrm{c}^3\,\mathrm{s} & -\mathrm{s}^3\mathrm{c} & 0 & 0 & 2(\mathrm{s}^3\mathrm{c} - \mathrm{c}^3\mathrm{s}) \\ \mathrm{s}^3\mathrm{c} & \mathrm{c}^3\mathrm{s} - \mathrm{s}^3\mathrm{c} & -\mathrm{c}^3\mathrm{s} & 0 & 0 & 2(\mathrm{c}^3\mathrm{s} - \mathrm{s}^3\mathrm{c}) \\ \mathrm{s}^2\mathrm{c}^2 & -2\mathrm{s}^2\mathrm{c}^2 & \mathrm{s}^2\mathrm{c}^2 & 0 & 0 & \mathrm{s}^4 + \mathrm{c}^4 - 2\mathrm{s}^2\mathrm{c}^2 \end{bmatrix}, \tag{B.10}$$

with

$$\mathrm{s} = \sin\alpha, \quad \mathrm{c} = \cos\alpha.$$

The definition of the angle α can be seen from Fig. B.1.
The midplane strains and curvatures of the right-hand side of Eq. (B.1) are expressed in terms of displacements.

[3]More generally speaking stiffness matrices are fourth-order tensors that can be transformed using the tensor transformation law $Q_{mnop} = Q^p_{ijkl} c_{mi} c_{nj} c_{ok} c_{pl}$, where the c's are the direction cosine [18].

In cylindrical coordinates the displacements in the axial, circumferential, and radial direction are $u, v,$ and w, respectively. The strain-displacement relations are derived for example by Flügge [33] or given by Whitney [21]:

$$\begin{aligned} \epsilon_x^0 &= \frac{\partial u^0}{\partial x} \,, & \kappa_x &= -\frac{\partial^2 w}{\partial x^2} \,, \\ \epsilon_\theta^0 &= \frac{1}{R}\left(\frac{\partial v^0}{\partial \theta} + w\right) \,, & \kappa_\theta &= -\frac{1}{R^2}\left(\frac{\partial^2 w}{\partial \theta^2} + w\right) \,, \\ \epsilon_{x\theta}^0 &= \frac{1}{R}\frac{\partial u^0}{\partial \theta} + \frac{\partial v^0}{\partial x} \,, & \kappa_{x\theta} &= -\frac{1}{R}\left(2\frac{\partial^2 w}{\partial x \partial \theta} + \frac{1}{R}\frac{\partial u^0}{\partial \theta} - \frac{\partial v^0}{\partial x}\right) \,. \end{aligned} \tag{B.11}$$

With the assumptions of plate and laminate laminate theory, the strain varies linearly with laminate thickness. Therefore, we can express the strains of the laminate as

$$\begin{pmatrix} \epsilon_x \\ \epsilon_\theta \\ \epsilon_{x\theta} \end{pmatrix} = \begin{pmatrix} \epsilon_x^0 \\ \epsilon_\theta^0 \\ \epsilon_{x\theta}^0 \end{pmatrix} + z \begin{pmatrix} \kappa_x \\ \kappa_\theta \\ \kappa_{x\theta} \end{pmatrix} , \tag{B.12}$$

where midplane strains and curvatures on the right-hand side are functions of the axial and the circumferential coordinate, only. The strain in the different plies varies linearly with laminate thickness.

From the equilibrium of forces on a volume element we get the following equations [33],[21]:

$$\frac{\partial N_x}{\partial x} + \frac{1}{R}\frac{\partial N_{x\theta}}{\partial \theta} = 0 \,, \tag{B.13}$$

$$\frac{\partial N_{x\theta}}{\partial x} + \frac{1}{R}\frac{\partial N_\theta}{\partial \theta} + \frac{1}{R}\frac{\partial M_{x_\theta}}{\partial x} + \frac{1}{R^2}\frac{\partial M_\theta}{\partial \theta} = 0 \,, \tag{B.14}$$

$$\frac{\partial^2 M_x}{\partial x^2} + \frac{2}{R}\frac{\partial^2 M_{x\theta}}{\partial x \partial \theta} + \frac{1}{R^2}\frac{\partial^2 M_\theta}{\partial \theta^2} - \frac{N_\theta}{R} = 0 \,. \tag{B.15}$$

For the **calculation of the displacements** of a laminate under thermal and mechanical loading, we have to know the temperature distribution in order to calculate the thermal forces according to Eq. (B.4). We then express the mechanical forces [Eq. (B.1)] in terms of thermal forces, elements of the stiffness matrix [Eq. (B.3)], and the unknown midplane strains and curvatures, written in terms of displacements according to Eq. (B.11). Substituting these expressions for the forces in Eqs. (B.13)–(B.15), we find three partial differential equations for the axial, the radial, and the circumferential displacements. These equations have to be solved with the appropriate boundary conditions.

Using the assumptions made in Section 3

$$A_{16} = A_{26} = D_{16} = D_{26} = 0 \,, \tag{B.16}$$

$$B = 0 \,, \tag{B.17}$$

$$v = 0 \,, \quad \text{and} \tag{B.18}$$

$$\frac{\partial(\ )}{\partial \theta} = 0 \,, \tag{B.19}$$

we obtain the **simplified equations**. From Eq. (B.11), we get:

$$\begin{aligned} \epsilon_x^0 &= \frac{\partial u^0}{\partial x} \,, & \kappa_x &= -\frac{\partial^2 w}{\partial x^2} \,, \\ \epsilon_\theta^0 &= \frac{1}{R}\, w \,, & \kappa_\theta &= -\frac{1}{R^2}\, w \,, \\ \epsilon_{x\theta}^0 &= 0 \,, & \kappa_{x\theta} &= 0 \,. \end{aligned} \tag{B.20}$$

With Eq. (B.1) and the above results, we obtain

$$\begin{pmatrix} N_x \\ N_\theta \\ N_{x\theta} \\ M_x \\ M_\theta \\ M_{x\theta} \end{pmatrix} = \begin{bmatrix} A_{11} & A_{12} & 0 & 0 & 0 & 0 \\ A_{12} & A_{22} & 0 & 0 & 0 & 0 \\ 0 & 0 & A_{66} & 0 & 0 & 0 \\ 0 & 0 & 0 & D_{11} & D_{12} & 0 \\ 0 & 0 & 0 & D_{12} & D_{22} & 0 \\ 0 & 0 & 0 & 0 & 0 & D_{66} \end{bmatrix} \begin{pmatrix} \epsilon_x^0 \\ \epsilon_\theta^0 \\ 0 \\ \kappa_x \\ \kappa_\theta \\ 0 \end{pmatrix} - \begin{pmatrix} N_x^\vartheta \\ N_\theta^\vartheta \\ 0 \\ M_x^\vartheta \\ M_\theta^\vartheta \\ 0 \end{pmatrix} , \tag{B.21}$$

and we see that

$$N_{x\theta} = M_{x\theta} = 0 \tag{B.22}$$

must hold. Using this together with the assumptions made ($v = 0$, and $\frac{\partial(\,)}{\partial\theta} = 0$), we get from Eqs. (B.13)–(B.15):

$$\frac{\partial N_x}{\partial x} = 0 , \tag{B.23}$$

$$0 = 0 ,$$

$$\frac{\partial^2 M_x}{\partial x^2} + \frac{N_\theta}{R} = 0 . \tag{B.24}$$

One of these equations is already fulfilled since we used the assumption $v = 0$.

We now express the forces and moments in Eqs. (B.23), (B.24) using Eq. (B.21), and we substitute the midplane strains and curvatures according to Eq. (B.20). We find two partial differential equations for u, and w:

$$A_{11}\frac{\partial^2 u^0}{\partial x^2} + A_{12}\frac{1}{R}\frac{\partial w}{\partial x} - \frac{\partial N_x^\vartheta}{\partial x} = \frac{\partial N_x}{\partial x} = 0 , \tag{B.25}$$

$$-D_{11}\frac{\partial^4 w}{\partial x^4} - D_{12}\frac{1}{R^2}\frac{\partial^2 w}{\partial x^2} - A_{22}\frac{1}{R^2}w - A_{12}\frac{1}{R}\frac{\partial u^0}{\partial x} = -\frac{1}{R}N_\theta^\vartheta + \frac{\partial^2 M_x^\vartheta}{\partial x^2} . \tag{B.26}$$

Integrating the first equation gives

$$A_{11}\frac{\partial u^0}{\partial x} + A_{12}\frac{1}{R}w - N_x^\vartheta = N_x = k_1 , \tag{B.27}$$

where the constant k_1 is given by the first boundary condition [see Eq. (3.4)]:

$$k_1 = F . \tag{B.28}$$

Solving Eq. (B.27) for $\partial u/\partial x$, and substituting this in the second equation, we get a fourth-order ordinary linear differential equation for the radial displacement:

$$A_1\frac{\partial^4 w}{\partial x^4} + A_2\frac{\partial^2 w}{\partial x^2} + A_3 w = -\frac{1}{R}N_\theta^\vartheta + \frac{\partial^2 M_x^\vartheta}{\partial x^2} + \frac{A_{12}}{A_{11}}\frac{1}{R}(N_x^\vartheta + F) , \tag{B.29}$$

where the temperature-dependent forces N_x^ϑ, and N_θ^ϑ are proportional to

$$\triangle\vartheta = \vartheta_c - \vartheta(x) = -a_\vartheta x^4 - b_\vartheta x^3 - c_\vartheta x^2 - d_\vartheta x + \vartheta_c - e_\vartheta , \tag{B.30}$$

and $\partial^2 M_x^\vartheta / \partial x^2$ is proportional to the second derivative of $\triangle\vartheta$.
In Eq. (B.30), $\vartheta(x)$ is the temperature of the tube as a function of x, calculated above [Eq. (A.7)], and ϑ_c is the laminate curing temperature which is a constant. The constants introduced in Eq. (B.29) are

$$A_1 = -D_{11} \ , \tag{B.31}$$

$$A_2 = -\frac{1}{R^2} D_{12} \ , \tag{B.32}$$

$$A_3 = -\frac{1}{R^2}\left(A_{22} + \frac{A_{12}^2}{A_{11}}\right) \ . \tag{B.33}$$

We write for the displacement in the radial direction

$$w = w_h + w_p \ , \tag{B.34}$$

where w_h is the solution of the homogeneous differential equation, and w_p a particular solution of the non-homogeneous differential equation. The solution is

$$w_h = \mathrm{e}^{\delta x} \ . \tag{B.35}$$

The characteristic polynomial

$$A_1\xi^4 + A_2\xi^2 + A_3 = 0 \ , \tag{B.36}$$

has in our case two pairs of conjugate complex solutions:

$$\begin{aligned} \xi_1 = a + ib \ , \quad \xi_2 = a - ib \ , \\ \xi_3 = -a + ib \ , \quad \xi_4 = -a - ib \ . \end{aligned} \tag{B.37}$$

According to Ref. [34], we can write for the solution

$$w_h = \mathrm{e}^{ax}(c_1 \ \sin(bx) + c_2 \ \cos(bx)) + \mathrm{e}^{-ax}(c_3 \ \sin(bx) + c_4 \ \cos(bx)) \ , \tag{B.38}$$

where c_1, c_2, c_3, and c_4 are constants.

The right-hand side of Eq. (B.29) can be written as a fourth- order polynomial (the thermal forces are proportional to $\triangle\vartheta$, otherwise there are only constants). Therefore, the particular solution is

$$w_p = a_w x^4 + b_w x^3 + c_w x^2 + d_w x + e_w \ . \tag{B.39}$$

Differentiating w_p four times, and substituting into the differential equation, we can determine the coefficients of w_p by comparing the coefficients with equal powers of x and solve for a_w, b_w, c_w, d_w, and e_w.
The complete solution for the radial displacement is the sum of the homogeneous and the particular solution according to Eq. (B.34)

$$\begin{aligned} w = \mathrm{e}^{ax}(c_1 \ \sin(bx) + c_2 \ \cos(bx)) + \mathrm{e}^{-ax}(c_3 \ \sin(bx) + c_4 \ \cos(bx)) + \\ a_w x^4 + b_w x^3 + c_w x^2 + d_w x + e_w \ . \end{aligned} \tag{B.40}$$

Substituting the solution for w in Eq. (B.27) and integrating this equation gives the solution for the displacement in the axial direction:

$$u^0(x) - u^0(0) = \frac{1}{A_{11}} \int_0^x \left(N_x^\vartheta + F - \frac{A_{12}}{R} w \right) \, \mathrm{d}x \; , \tag{B.41}$$

where the term $u^0(0)$ that occurs on the left-hand side is zero according to the boundary conditions [see Eq.(3.4)] in Section 3.
There are four boundary conditions for the four constants c_1,..., c_4. They can be formulated using Eqs. (B.41),(B.40), and for the last two boundary conditions using Eq. (B.21, B.20) as well. This results in a system of four linear equations for the four constants.

Once these four constants are known, the midplane strains and curvatures are used to calculate the strains in each ply with the assumption of laminate theory that strain varies linearly over laminate thickness [Eq. (B.12)]. This gives the strains in the global coordinate system (x, θ, z-system).

In order to get the strains in the coordinate system of each ply (superscript p), we have to transform the strains from the global coordinate system, to the coordinate system of each ply, using

$$\epsilon_i^p = T_{ij} \epsilon_j; \;\; i = 1, 2, 6 \; , \tag{B.42}$$

where

$$T = \begin{pmatrix} \cos^2 \alpha & \sin^2 \alpha & \cos \alpha \, \sin \alpha \\ \sin^2 \alpha & \cos^2 \alpha & -\cos \alpha \, \sin \alpha \\ -2 \cos^2 \alpha & -2 \sin^2 \alpha & \cos^2 \alpha - \sin^2 \alpha \end{pmatrix} \tag{B.43}$$

is the transformation matrix used for the engineering strains, with α according to Fig. B.1.

We can now calculate the ply stress in the fibre direction (σ_1) and in the transverse direction (σ_2), and the in-plane shear stress ($\sigma_6 = \tau_{12}$) using

$$\sigma_i^p = Q_{ij}^p (\epsilon_j^p - \epsilon_j^{p,\vartheta}); \;\; i = 1, 2, 6 \; , \tag{B.44}$$

with Q^p given in Eq. (B.7).
The ply stresses and strains as a function of the axial coordinate are shown in Fig. 3.3.
The program code (Matlab) is given in Appendix C.

Appendix C: Program Codes

Temperature Distribution

Matlab M-File ”solofde.m”

```
%%%%%%%%%%%%%%%%%%%%%%%%%%%%%%%%%%%%%%%%%%%%%%%%%%%%
%
%  Iterative Solution of D.E. of Conduction of Heat
%                 "solofde.m"
%          Gero Pflanz, CERN, March 97
%                 SL-Division
%                   RF-Group
%
%%%%%%%%%%%%%%%%%%%%%%%%%%%%%%%%%%%%%%%%%%%%%%%%%%%%%%
%
% governing Equation: -lambda(T)*dT/dx = const = qpkt
%
%%%%%%%%%%%%%%%%%%%%%%%%%%%%%%%%%%%%%%%%%%%%%%%%%%%%%%
%
% This file requires the files
%
% - curfi1.m
% - curfi2.m
% - d_e.m
% - lambda_T.m
%
% in the same directory
%
%
% effective length of tube in meters

l = 0.25

% diameters of tube in m

% inner diameter

di =  0.055

% outer diameter

da = 0.061

% Temperatur at both ends of tube in Kelvin

T1 = 15
T2 = 290
global T1;

% Cross-Section of Tube

A_s = pi/4*(daˆ2-diˆ2)


%%%%%%%%%%%%%%%%%%%%%%%%%%%%%%%%%%%%%%%%%%%%%%%%%%%%%%%
%
% Curve-Fit to experimental Data,
% Thermal Conductivity as a Function of
% Temperature
%
% lambda(T) = a1(1) + a1(2)*T + a1(3)*Tˆ2 + a1(4)*Tˆ3
% table of measured heat conduction coefficients
%
%%%%%%%%%%%%%%%%%%%%%%%%%%%%%%%%%%%%%%%%%%%%%%%%%%%%%%%

% Experimental Data, Temperatures in [K],
% lambda in [W/(Km)]

T        = [  20   30   40   50   60...
   80  100   200   300];
lambda_T = [0.17 0.28 0.43 0.61 0.80...
 1.18 1.64  3.63  5.02];


% Parameters for Algorithm

opti=foptions;
opti(2)=1e-9;
opti(3)=1e-9;
opti(7)=1;
opti(14)=1000;

% Starting guess

a1 = 0
b1 = 0.0001
c1 = 0.01
d1 = -0.04

a1vect = fmins(’curfi1’,[a1 b1 c1 d1],opti);

a1 = a1vect(1)
b1 = a1vect(2)
c1 = a1vect(3)
d1 = a1vect(4)

global a1vect;

% plot of Curve Fit and exp. data

hold off
ti=1:310;
plot(ti,d1+c1*ti+b1*ti.ˆ2+a1*ti.ˆ3,’g’);  % Fit
hold on
axis([10 310 0 5.1])
plot(T,lambda_T,’or’);                          % Measurement
hold on
title([’Coefficients of Heat - Conduction over absolute...
 Temperature’]);
xlabel([’  Temperature                      [K]’]);
ylabel([’  Coefficient of Heat Conduction   [W/(mK)]’]);
grid on

% Calculation of Heat flow through Tube

Qpkt = -A_s/l*quad8(’lambda_T’,T1,T2)  % Integration
qpkt = Qpkt/A_s;

global qpkt;

% Solution of D.E. using Newtons Method,
% Temperature calculated for each millimeter of tube length

T=T2;
global x;
for x=l:-0.001:0.0
  T=fzero(’d_e’,T);
  Tc(x*1000+1)=T;
end

Tgl = Tc;
lgl = [0.0:0.001:l];
global lgl Tgl;

%%%%%%%%%%%%%%%%%%%%%%%%%%%%%%%%%%%%%%%%%%%%%%%%%%%%%%%
%
% Curve-Fit to the iterative Solution of the,
% Differential Equation.
% Temperature as a function of tube-length
%
% T = T1 + d*x + c*xˆ2 + b*xˆ3 + a*xˆ4
%
%%%%%%%%%%%%%%%%%%%%%%%%%%%%%%%%%%%%%%%%%%%%%%%%%%%%%%%

% Starting guess

a = -319121;
b = 186652;
c = -38753;
d = 4075.7;


a2vect = fmins(’curfi2’,[a b c d],opti);

global a2vect;

a = a2vect(1)
b = a2vect(2)
c = a2vect(3)
d = a2vect(4)

global a1vect;


hold off
ti=0:0.001:0.25;
plot(ti,T1+d*ti+c*ti.ˆ2+b*ti.ˆ3+a*ti.ˆ4,’y’);  % Fit
hold on
axis([0 0.250 0 300])
plot(ti,Tgl(ti*1000+1),’y.’);            % Solution
hold on
title([’Temperature over Tube-Length, Iterative Solution...
 and Curve Fit’]);
ylabel([’Temperature ("-" = Iter. Sol. of D.E.,".-" = ...
Curve Fit to Sol.) [K]’]);
xlabel([’ Effective Tube Length in meters   [m]’]);
grid on

% Save Coefficients of Curve Fit for Stress-Strain...
 Calculations

save c:\temp\coeff a2vect
```

Matlab Sub-Routine ”curfi1.m”

```
% Curve Fit to experimental data,
% Thermal conductivity as a function of temperature
```

```
function te = curfi1(lam)

% Extrapolated experimental data (Temperature and
% Coefficient of Thermal Conductivity)

T        = [  20   30   40   50   60...
   80  100   200   300];
lambda_T = [0.17 0.28 0.43 0.61 0.80...
 1.18 1.64  3.63  5.02];

% Function chosen for Curve Fit

y = lam(4) + lam(3)*T +lam(2)*T.^2+lam(1)*T.^3;

% Error as the sum of the distances of the measured point,
% from the point of the fitted curve

e=0;
for a=1:length(T)
  e = e+(lambda_T(a)-y(a))^2;
end
te=e
```

Matlab Sub-Routine ”curfi2.m”

```
% Curve Fit through iterative solution of the
% D.E. of conduction of heat

function te = curfi2(lam)
global lgl Tgl T1;

% Function chosen for Curve Fit

y = T1 + lam(4)*lgl+lam(3)*lgl.^2+...
lam(2)*lgl.^3+lam(1)*lgl.^4;

% Error

e=0;
for a=1:length(Tgl)
  e = e+(Tgl(a)-y(a))^2;
end
te=e
```

Matlab Sub-Routine ”d_e.m”

```
function zero = x_T(T)

global qpkt x T1 a1vect;
zero = - quad('lambda_T',T1,T)/qpkt - x;
```

Matlab Sub-Routine ”lambda_T.m”

```
function y = lambda_T(t)
global a1vect;
y = a1vect(4) + a1vect(3)*t +...
 a1vect(2)*t.^2 + a1vect(1)*t.^3;
```

Stress Analysis

```
%%%%%%%%%%%%%%%%%%%%%%%%%%%%%%%%%%%%%%%%%%%%%%%%%%%%%%%%%%%%
%
%  PLYSTR.M
%
%%%%%%%%%%%%%%%%%%%%%%%%%%%%%%%%%%%%%%%%%%%%%%%%%%%%%%%%%%%%
%
% M-File for calculation of Stiffness-Matrices,
% and Stress-Strain Distribution
% For Carbon-Fibre Reinforced Tube for Tuner
% Gero Pflanz, April 1997
% CERN
%
%%%%%%%%%%%%%%%%%%%%%%%%%%%%%%%%%%%%%%%%%%%%%%%%%%%%%%%%%%%%

% Ply-constants

E11 = 143500000000
E22 =   9500000000
v12 = 0.32
v21 = 0.021
G12 =   6150000000
al11 = -8.0E-7
al22 =  3.7E-5
SL =    2550000000
ST =      68000000
SS =      80000000

% mechanical load, x-direction

% divided by cross-section

sigman = 54000000;

% Layers coordinates, thickness, over all radius,
% tube length (meters)

h = -0.0015:0.00075:0.0015
t = 0.003
R = 0.029
L = 0.25

% Winding angle

alpha = 18

% Load cefficients of temperature polynomial
% deltaT(x)=At*x^4+Bt*x^3+Ct*x^2+Dt*x+Et

load c:\temp\co

% Curing Temperature

Tcur=385

At = a2vect(1)
Bt = a2vect(2)
Ct = a2vect(3)
Dt = a2vect(4)
Et = 15-Tcur

% Loop to calculate stresses for different winding angles

for alpha = 1:1:90

% ply-stiffness matrix in ply-coordinate system

q11 = E11 / (1 - v12*v21);
q22 = E22 / (1 - v12*v21);
q12 = v12*E22 / (1 - v12*v21);
q12 = v21*E11 / (1 - v12*v21);
q66 = G12;

Q = [ q11 q12 0 ; q12 q22 0 ; 0 0 q66 ];

u1 = 1/8*(3*q11 +3*q22 +2*q12+4*q66);
u2 = 1/2*(q11-q22);
u3 = 1/8*(q11+q22-2*q12-4*q66);
u4 = 1/8*(q11+q22+6*q12-4*q66);
u5 = 1/2*(u1-u4);

% Transformation to global coordinate system, for both ply
% orientations

theta = alpha*pi/180;

s2t = sin(2*theta);
s4t = sin(4*theta);
c2t = cos(2*theta);
c4t = cos(4*theta);

qp11 = u1 + u2*c2t + u3*c4t;
qp12 = u4 - u3*c4t;
qp22 = u1 - u2*c2t + u3*c4t;
qp16 = 1/2*u2*s2t + u3*s4t;
qp26 = 1/2*u2*s2t - u3*s4t;
qp66 = u5 - u3*c4t;

Qp = [qp11 qp12 qp16 ; qp12 qp22 qp26 ; qp16 qp26 qp66];
Sp = inv (Qp);

c2=(cos(theta))^2;
s2=(sin(theta))^2;
sc = sin(theta) * cos(theta);
al11;
al22;
alp(1) = al11 * c2 + al22*s2;
alp(2) = al11 * s2 + al22*c2;
alp(3) = 2 * sc * (al11-al22);

%%%%%%%%%%%%%%%%%%%%%%%%%%%%%%%%%%%%%%%%%%%%%%%%%%%%%%%%%%%%

theta = -alpha*pi/180;

s2t = sin(2*theta);
s4t = sin(4*theta);
c2t = cos(2*theta);
c4t = cos(4*theta);

qm11 = u1 +u2*c2t + u3*c4t;
qm12 = u4 - u3*c4t;
qm22 = u1 - u2*c2t + u3*c4t;
qm16 = 1/2*u2*s2t + u3*s4t;
qm26 = 1/2*u2*s2t - u3*s4t;
qm66 = u5 - u3*c4t;
```

```
Qm = [qm11 qm12 qm16 ; qm12 qm22 qm26 ; qm16 qm26 qm66];
Sm = inv (Qm);

c2=(cos(theta))^2;
s2=(sin(theta))^2;
sc = sin(theta) * cos(theta);

alm(1) = al11 * c2 + al22*s2;
alm(2) = al11 * s2 + al22*c2;
alm(3) = 2 * sc * (al11-al22);

%%%%%%%%%%%%%%%%%%%%%%%%%%%%%%%%%%%%%%%%%%%%%%%
%%%%%%%%%%%%%%%%%%%%%%%%%%%%%%%%%%%%%%%%%%%%%%%

% Calculation of laminates stiffness matrices

for m = 1 : 3
  for n = 1 : 3
    A(m,n) = Qp(m,n) * (h(2)-h(1)) +...
     Qm(m,n) * (h(3)-h(2)) +...
     Qp(m,n) * (h(4)-h(3)) +...
     Qm(m,n) * (h(5)-h(4));
    D(m,n) = 1/3*(...
     Qp(m,n) * ((h(2))^3 - (h(1))^3) +...
          Qm(m,n) * ((h(3))^3 - (h(2))^3) +...
          Qp(m,n) * ((h(4))^3 - (h(3))^3) +...
     Qm(m,n) * ((h(5))^3 - (h(4))^3)...
     );
  end
end
B=[[0 0 0];[0 0 0];[0 0 0]];

% Laminate Stiffness matrices, and inverse

AI=inv(A);
DI=inv(D);

AA=[[A B];[B D]];
AAI=inv(AA);


% Calculation of thermal forces

  Ts(1) =  2 * (h(2) - h(1)) * (Qp(1,1)*alp(1) +...
        Qp(1,2)*alp(2) + Qp(1,3)*alp(3)) +...
           2 * (h(3) - h(2)) * (Qm(1,1)*alm(1) +...
             Qm(1,2)*alm(2) + Qm(1,3)*alm(3));
  Ts(2) =  2 * (h(2) - h(1)) * (Qp(2,1)*alp(1) +...
        Qp(2,2)*alp(2) + Qp(2,3)*alp(3)) +...
           2 * (h(3) - h(2)) * (Qm(2,1)*alm(1) +...
             Qm(2,2)*alm(2) + Qm(2,3)*alm(3));
  Ts(3)=0;  % Orthotropes Rohr

  Tss(1) =1/2*(...
           ((h(2))^2 - (h(1))^2)*(Qp(1,1)*alp(1) +...
              Qp(1,2)*alp(2) + Qp(1,3)*alp(3)) +...
   ((h(3))^2 - (h(2))^2)*(Qm(1,1)*alm(1) +...
      Qm(1,2)*alm(2) + Qm(1,3)*alm(3)) +...
   ((h(4))^2 - (h(3))^2)*(Qp(1,1)*alp(1) +...
      Qp(1,2)*alp(2) + Qp(1,3)*alp(3)) +...
   ((h(5))^2 - (h(4))^2)*(Qm(1,1)*alm(1) +...
      Qm(1,2)*alm(2) + Qm(1,3)*alm(3)));
  Tss(2) =1/2*(...
           ((h(2))^2 - (h(1))^2)*(Qp(2,1)*alp(1) +...
              Qp(2,2)*alp(2) + Qp(2,3)*alp(3)) +...
   ((h(3))^2 - (h(2))^2)*(Qm(2,1)*alm(1) +...
      Qm(2,2)*alm(2) + Qm(2,3)*alm(3)) +...
   ((h(4))^2 - (h(3))^2)*(Qp(2,1)*alp(1) +...
      Qp(2,2)*alp(2) + Qp(2,3)*alp(3)) +...
   ((h(5))^2 - (h(4))^2)*(Qm(2,1)*alm(1) +...
      Qm(2,2)*alm(2) + Qm(2,3)*alm(3)));
  Tss(3)=0;  % Orthotropes Rohr

% Thermal forces divided by deltaT(x)

nth=Ts;
mth=Tss;
Nme = [sigman*t 0 0 0 0 0];
N = Nth + Nme;

%%%%%%%%%%%%%%%%%%%%%%%%%%%%%%%%%%%%%%%%%%%%%%%%%%%
%
%    Solving for Displacements u und w
%
%%%%%%%%%%%%%%%%%%%%%%%%%%%%%%%%%%%%%%%%%%%%%%%%%%%

% Solving the homogeneous differential equation

A1 = -D(1,1);
A2 = -D(1,2)/(R^2);
A3 = -1/(R^2)*(A(2,2)-(A(1,2)^2)/A(1,1));

% a,b aus charakteristischem Polynom der Homogenen DGl.

rho1 = -A2/(2*A1) + ( A2^2/(4*A1^2) - A3/A1)^0.5;
rho2 = -A2/(2*A1) - ( A2^2/(4*A1^2) - A3/A1)^0.5;
```

```
lambda1 =  (rho1)^0.5;
lambda2 =  (rho2)^0.5;
lambda3 = -(rho1)^0.5;
lambda4 = -(rho2)^0.5;

a = abs(real(lambda1));
b = abs(imag(lambda1));

% Solving the partial differential equation

Kst = (-nth(2)/R + A(1,2)/(A(1,1)*R) * nth(1) );
Kstst = Nme(1) * A(1,2) / (A(1,1)*R);

% Coefficients of the partial solution

Ap = Kst*At/A3;
Bp = Kst*Bt/A3;
Cp = (Kst*Ct + mth(1)*12*At - 12*Ap*A2)/A3;
Dp = (Kst*Dt + mth(1)*6*Bt -   6*Bp*A2)/A3;
Ep = (Kst*Et + mth(1)*2*Ct -   2*Cp*A2 - 24*Ap*A1 + Kstst)/A3;

%%%%%%%%%%%%%%%%%%%%%%%%%%%%%%%%%%%%%%%%%%%%%%%%%%%%%%
%
%  Calculation of displacements and their derivatives
%
%%%%%%%%%%%%%%%%%%%%%%%%%%%%%%%%%%%%%%%%%%%%%%%%%%%%%%

% Abbriviations

ALB = At*L^4 + Bt*L^3 + Ct*L^2 + Dt*L + Et;

eal = exp(a*L);
emal = exp(-a*L);

sbl = sin(b*L);
cbl = cos(b*L);

a2mb2 = a^2 - b^2;
a2b2 = a^2 + b^2;

ab2 = 2*a*b;

ab2sbl = ab2*sbl;
ab2cbl = ab2*cbl;

% System of linear equations for the constants

K10 = mth(1)*Et + D(1,2)/(R^2)*(Ep) +...
 D(1,1)*(2*Cp);
K11 = -ab2*D(1,1);
K12 = -a2mb2*D(1,1) - D(1,2)/(R^2);
K13 = ab2*D(1,1);
K14 = -a2mb2*D(1,1) - D(1,2)/(R^2);


K20 = ( nth(2)*Et - A(1,2)/A(1,1) *...
      ( nth(1)*Et + Nme(1) )) *...
      R/(A(2,2)-(A(1,2)^2)/A(1,1)) - Ep;
K21 = 0;
K22 = 1;
K23 = 0;
K24 = 1;


K30 = ( nth(2)*ALB - A(1,2)/A(1,1) *...
      ( nth(1)*ALB + Nme(1) ))*...
      R/(A(2,2)-(A(1,2)^2)/A(1,1)) -...
      Ap*L^4 - Bp*L^3 -...
      Cp*L^2 - Dp*L - Ep;
K31 = eal*sbl;
K32 = eal*cbl;
K33 = emal*sbl;
K34 = emal*cbl;

K40 = mth(1)*ALB + D(1,2)/(R^2)*...
         (Ap*L^4 + Bp*L^3 + Cp*L^2 +...
         Dp*L + Ep) + D(1,1)*...
        (12*Ap*L^2 + 6*Bp*L + 2*Cp);
K41 = (a2mb2*sbl + ab2cbl)*eal*(-D(1,1)) -...
                 D(1,2)/(R^2)*sbl*eal;
K42 = (a2mb2*cbl - ab2sbl)*eal*(-D(1,1)) -...
                 D(1,2)/(R^2)*cbl*eal;
K43 = (a2mb2*sbl - ab2cbl)*emal*(-D(1,1)) -...
                 D(1,2)/(R^2)*sbl*emal;
K44 = (a2mb2*cbl + ab2sbl)*emal*(-D(1,1)) -...
                 D(1,2)/(R^2)*cbl*emal;


RS = [K10 K20 K30 K40]’;
K  = [[K11 K12 K13 K14];...
      [K21 K22 K23 K24];...
      [K31 K32 K33 K34];...
      [K41 K42 K43 K44]];

KM1 = inv(K);
```

```
% Solving for the constants

CV = KM1*RS;

%%%%%%%%%%%%%%%%%%%%%%%%%%%%%%%%%%%%%%%%%%%%%%%%%%%%%%%%%%%%%%%%%%%%%%%%%%%%
%
%  Calculation of displacements and their derivatives, and
%  the ply-strains in the global coordinate system
%
%%%%%%%%%%%%%%%%%%%%%%%%%%%%%%%%%%%%%%%%%%%%%%%%%%%%%%%%%%%%%%%%%%%%%%%%%%%%

for i=1:250
x=i/1000;
   w(i) = exp(a*x)*( CV(1)*sin(b*x)+CV(2)*cos(b*x) ) +...
          exp(-a*x)*( CV(3)*sin(b*x)+CV(4)*cos(b*x) ) +...
  Ap*x^4 + Bp*x^3 + Cp*x^2 + Dp*x + Ep;
   dwdx(i) =   exp(a*x)*(...
 sin(b*x)*(CV(1)*a-b*CV(2))+...
 cos(b*x)*(CV(2)*a+b*CV(1))...
       ) +...
              exp(-a*x)*(...
 sin(b*x)*(-CV(3)*a-b*CV(4))+...
   cos(b*x)*(-CV(4)*a+b*CV(3)))...
       ) +...
       4*Ap*x^3 + 3*Bp*x^2 + 2*Cp*x + Dp;
   d2wdx2(i) = exp(a*x)*(...
 sin(b*x)*(CV(1)*a^2-2*CV(2)*a*b-CV(1)*b^2) +...
    cos(b*x)*(CV(2)*a^2+2*CV(1)*a*b-CV(2)*b^2)...
       ) + ...
       exp(-a*x)*(...
 sin(b*x)*(CV(3)*a^2+2*CV(4)*a*b-CV(3)*b^2) +...
    cos(b*x)*(CV(4)*a^2-2*CV(3)*a*b-CV(4)*b^2)...
       ) +...
      12*Ap*x^2 + 6*Bp*x + 2*Cp;

   u(i) = ( nth(1)*(At/5*x^5 + Bt/4*x^4 + Ct/3*x^3 +...
            Dt/2*x^2 + Et*x) +...
            Nme(1)*x ) /A(1,1)-...
            A(1,2)/(A(1,1)*R)* (...
exp(a*x)/a2b2*( CV(1)*a*sin(b*x) -...
                CV(1)*b*cos(b*x) ) +...
exp(a*x)/a2b2*( CV(2)*a*cos(b*x) +...
                CV(2)*b*sin(b*x) ) +...
exp(-a*x)/a2b2*(-CV(3)*a*sin(b*x) -...
                 CV(3)*b*cos(b*x) ) +...
exp(-a*x)/a2b2*(-CV(4)*a*cos(b*x) +...
                 CV(4)*b*sin(b*x) ) +...
    Ap/5*x^5 + Bp/4*x^4 + Cp/3*x^3 + Dp/2*x^2 +...
    Ep*x -((-CV(1)*b + CV(2)*a - CV(3)*b -...
    CV(4)*a) /a2b2 ));

   dudx(i) = ( nth(1)*( At*x^4 + Bt*x^3 +...
           Ct*x^2 + Dt*x + Et)+...
       Nme(1)-A(1,2)*w(i)/R ) /A(1,1);

% Ply strains of midplane, upper layer, and lower layer

   epsix0(i) = dudx(i);
   epsixu(i) = dudx(i) + 0.0015*d2wdx2(i);
   epsixo(i) = dudx(i) - 0.0015*d2wdx2(i);
   epsith0(i) = w(i)/R;
   epsithu(i) = w(i)/R + 0.0015*w(i)/(R^2);
   epsitho(i) = w(i)/R - 0.0015*w(i)/(R^2);
   epsixth(i)=0;

end

% Calculation of ply stresses in ply-coordinate system

theta = alpha*pi/180;

c2=(cos(theta))^2;
s2=(sin(theta))^2;
sc = sin(theta) * cos(theta);
cs=sc;

TFp = [[c2 s2 cs];[s2 c2 -cs];[-2*cs 2*cs c2-s2]];

epsix=[[epsix0];[epsith0];[epsixth]];

for i=1:250
  it=i/1000;
  sigm12(1:3,i) = Q*(TFp*epsix(1:3,i)-...
       (At*it^4+Bt*it^3+...
       Ct*it^2+Dt*it+Et)*...
       [al11 al22 0]');
end

epsixob=[[epsixo];[epsitho];[epsixth]];

for i=1:250
  it=i/1000;
  sigm12ob(1:3,i) = Q*(TFp*epsixob(1:3,i)-...
        (At*it^4+Bt*it^3+Ct*it^2+...
                 Dt*it+Et)*...
[al11 al22 0]');
end

epsixun=[[epsixu];[epsithu];[epsixth]];

for i=1:250
  it=i/1000;
  sigm12un(1:3,i) = Q*(TFp*epsixun(1:3,i)-...
        (At*it^4+Bt*it^3+Ct*it^2+...
                 Dt*it+Et)*...
[al11 al22 0]');
end

% Factor to transform units from N/m^2 to MPa

facM = 1E6;

% Plot Ply-stresses, over tube length

hold off
plot(sigm12(1,:)/facM,'y'); hold on
plot(sigm12(2,:)/facM,'b');
plot(-sigm12(3,:)/facM,'r');
plot(sigm12ob(1,:)/facM,'y--');
plot(sigm12ob(2,:)/facM,'b--');
plot(-sigm12ob(3,:)/facM,'r--');
plot(sigm12un(1,:)/facM,'y.');
plot(sigm12un(2,:)/facM,'b.');
plot(-sigm12un(3,:)/facM,'r.');
title(['Ply Stresses in inner Ply (.), outer '...
       'Ply (-.), and Midplane (-);+-18 degree;'...
       ' 2.5 kN;dT=-370/-110, RB']);
ylabel(['Different Ply-Stresses in MPa']);
xlabel(['Tube Length in mm']);
grid on

%%%%%%%%%%%%%%%%%%%%%%%%%%%%
%
% Calculate Safety Factors
%
%%%%%%%%%%%%%%%%%%%%%%%%%%%%

axis([0 250 -10 70]);
Smaxob=0;
for i=1:250
  Sa=(sigm12ob(1,i)/SL)^2-...
      sigm12ob(1,i)*sigm12ob(2,i)/(SL)^2+...
     (sigm12ob(2,i)/ST)^2+...
     (sigm12ob(3,i)/SS)^2;
  if Sa>Smaxob
    Smaxob = Sa;
    imaxob =i;
  end
end

imaxob
Smaxob

Smaxun=0;
for i=1:250
  Sa=(sigm12un(1,i)/SL)^2-...
      sigm12un(1,i)*sigm12un(2,i)/(SL)^2+...
     (sigm12un(2,i)/ST)^2+...
     (sigm12un(3,i)/SS)^2;
  if Sa>Smaxun
    Smaxun = Sa;
    imaxun=i;
  end
end

imaxun
Smaxun

Smax=0;
for i=1:250
  Sa=(sigm12(1,i)/SL)^2-...
      sigm12(1,i)*sigm12(2,i)/(SL)^2+...
     (sigm12(2,i)/ST)^2+...
     (sigm12(3,i)/SS)^2;
  if Sa>Smax
    Smax = Sa;
    imax=i;
  end
end

imax
Smax

i=1
  S1(alpha)=(sigm12ob(1,i)/SL)^2 -...
             sigm12ob(1,i)*sigm12ob(2,i)/((SL)^2)+...
            (sigm12ob(2,i)/ST)^2 +...
            (sigm12ob(3,i)/SS)^2;
i=30;
  S30(alpha)=(sigm12ob(1,i)/SL)^2 -...
              sigm12ob(1,i)*sigm12ob(2,i)/((SL)^2)+...
             (sigm12ob(2,i)/ST)^2 +...
```

```
            (sigm12ob(3,i)/SS)^2;
i=250;
  S250(alpha)=(sigm12ob(1,i)/SL)^2 -...
               sigm12ob(1,i)*sigm12(2,i)/((SL)^2)+...
              (sigm12ob(2,i)/ST)^2 +...
              (sigm12ob(3,i)/SS)^2;

alpha

% end of loop for different winding angles

end
```